J. Fluid Mech. (2021), *vol*. 927, A31, doi:10.1017/jfm.2021.756

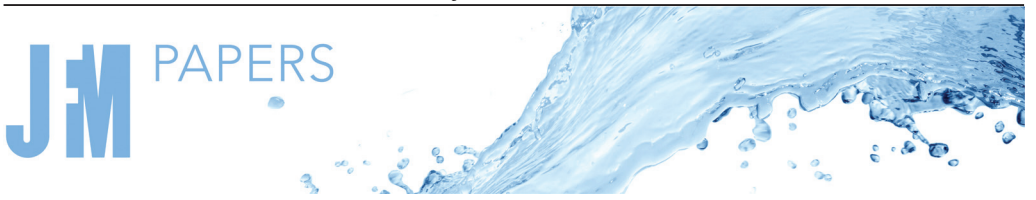

Homogenization-based design of microstructured membranes: wake flows past permeable shells

Pier Giuseppe Ledda[1,†], **E. Boujo**[1], **S. Camarri**[2], **F. Gallaire**[1] **and G.A. Zampogna**[1]

[1]Laboratory of Fluid Mechanics and Instabilities, École Polytechnique Fédérale de Lausanne, CH-1015 Lausanne, Switzerland

[2]Dipartimento di Ingegneria Civile e Industriale, Università degli Studi di Pisa, 56122 Pisa, Italy

(Received 15 April 2021; revised 1 July 2021; accepted 19 August 2021)

A formal framework to characterize and control/optimize the flow past permeable membranes by means of a homogenization approach is proposed and applied to the wake flow past a permeable cylindrical shell. From a macroscopic viewpoint, a Navier-like effective stress jump condition is employed to model the presence of the membrane, in which the normal and tangential velocities at the membrane are respectively proportional to the so-called filtrability and slip numbers multiplied by the stresses. Regarding the particular geometry considered here, a characterization of the steady flow for several combinations of constant filtrability and slip numbers shows that the flow morphology is dominantly influenced by the filtrability and exhibits a recirculation region that moves downstream of the body and eventually disappears as this number increases. A linear stability analysis further shows the suppression of vortex shedding as long as large values of the filtrability number are employed. In the control/optimization phase, specific objectives for the macroscopic flow are formulated by adjoint methods. A homogenization-based inverse procedure is proposed to obtain the optimal constrained microscopic geometry from macroscopic objectives, which accounts for fast variations of the filtrability and slip profiles along the membrane. As a test case for the proposed design methodology, a cylindrical membrane is designed to maximize the resulting drag coefficient.

Key words: flow control, membranes, porous media

† Email address for correspondence: pier.ledda@epfl.ch

1. Introduction

The behaviour of wake flows past permeable bodies and membranes is of considerable interest owing to its large range of applications, in both nature and engineering. Several insects, such as thrips and wasps, present bristled wings, offering a considerable aerodynamic benefit when compared with impervious wings in terms of propulsion efficiency per unit weight of the wing itself (Ellington 1980; Barta & Weihs 2006; Jones *et al.* 2016). Owls are renowned for their silent flight, which stems from the particular microscopic permeable structure of the hair composing the wings (Wagner *et al.* 2017; Jaworski & Peake 2020). Dandelion seeds are transported in the air by a structure called pappus, which behaves as a parachute. The presence of voids markedly decreases the falling velocity and stabilizes the steady flow (Cummins *et al.* 2018; Ledda *et al.* 2019). At smaller scales, thin permeable shells are of essential importance for unicellular organisms as a key point in their displacement and feeding strategies (Asadzadeh *et al.* 2019). Within the vascular system of plants, permeable microstructures called sieve plates are crucial for sap translocation (Jensen *et al.* 2016).

In addition to these natural examples, there are several industrial applications concerning flows through permeable structures with a plethora of microscopic properties and pore sizes, ranging from millimetres for particle filtration to nanometres for desalination (Fritzmann *et al.* 2007; Elimelech & Phillip 2011; Matin *et al.* 2011) and wastewater recovery (Shannon *et al.* 2008; Rahardianto, McCool & Cohen 2010). At larger scales, the flow around permeable bluff bodies, such as parachutes and nets, is gaining more and more interest (Cummins *et al.* 2018; Labbé & Duprat 2019). Fog water harvesting systems, particularly employed in arid climates (Olivier 2004; Labbé & Duprat 2019), are built using either nets (Park *et al.* 2013) or harps (Shi *et al.* 2018; Labbé & Duprat 2019).

In these last examples, a deep understanding of aerodynamic flows investing permeable structures is crucial and, for decades, the uniform flow past a solid or porous circular cylinder has been the testing ground to train the understanding of flows around bluff bodies. The flow past a solid circular cylinder is steady for low values of the Reynolds number. The steadiness of the wake is broken at a critical Reynolds number of 46.7 (Jackson 1987; Provansal, Mathis & Boyer 1987), beyond which the flow undergoes an instability that leads to a two-dimensional oscillatory flow characterized by the alternate shedding of vortices, i.e. the renowned von Kármán vortex street (Williamson 1996). At larger Reynolds numbers $Re \approx 192$, the two-dimensional wake becomes unstable and three-dimensional structures develop, whose characteristic trace is still the two-dimensional alternate shedding of vortices (Barkley & Henderson 1996). The sequence of bifurcations that a flow may encounter can be approached in the context of bifurcation theory and linear stability analysis (Chomaz 2005; Theofilis 2011). These methods are now largely employed and their reliability in the prediction of instability thresholds and shedding frequencies close to the threshold (Barkley 2006) is now well assessed, spanning different length scales, from microfluidics systems (Bongarzone *et al.* 2021) to bluff body aerodynamics (Meliga, Chomaz & Sipp 2009) and industrial applications such as wind and hydraulic turbines (Iungo *et al.* 2013; Viola *et al.* 2014; Pasche, Avellan & Gallaire 2017).

A largely investigated field in fluid dynamics is the control of flow instabilities. One of the first studies of the control of the von Kármán vortex street via modifications of the solid surface and velocity can be traced back to Prandtl, who controlled the flow past a circular cylinder using the blowing effect of a small hole on the surface (Willert *et al.* 2019). Castro (1971) studied experimentally the flow around perforated flat plates for Reynolds numbers of order 10^4, finding that the vortex shedding was inhibited if the voids-to-material ratio

(porosity) is sufficiently large. Two different regimes were distinguished: a solid behaviour in which the von Kármán vortex street is present, with a downstream displacement of the mean recirculation region and the vortex formation region, and a regime in which the vortex shedding is quenched. Zong & Nepf (2012) performed an experimental study of circular cylinders composed of arrays of smaller cylinders, for Reynolds numbers of order 10^4, showing that also in this case the von Kármán vortex street was inhibited for large porosities, with results similar to those of the numerical study of Nicolle & Eames (2011). Recently, Steiros & Hultmark (2018) developed a theoretical framework to evaluate the drag coefficient behaviour for flat perforated plates, for Reynolds numbers of the order of 10^3. In a similar investigation of circular perforated plates, Steiros *et al.* (2020) also showed how variable distributions of holes may strongly modify the flow morphology and the resulting aerodynamic forces. Other analytical investigations of the aerodynamic forces on porous airfoils have been performed by Hajian & Jaworski (2017) and Baddoo, Hajian & Jaworski (2021). In Hajian & Jaworski (2017) a potential flow model to evaluate the aerodynamic forces on thin permeable airfoils was proposed. The presence of a porous structure was described by a seepage flow rate through the permeable surface. Baddoo *et al.* (2021) generalized this analysis to the unsteady case such as pitching and heaving motion or gust loads. Other experimental investigations focused on the drag variation of porous disks at low Reynolds numbers (Strong *et al.* 2019) and on the fluid–structure interaction of porous flexible strips (Pezzulla *et al.* 2020), to name a few. Ledda *et al.* (2018) performed a study of the effect of permeability on the stability of the steady and two-dimensional flow around porous rectangles, obtaining a general permeability threshold beyond which the wake is steady.

In the works cited above, two essentially different ways to model porous structures can be distinguished. Pore-scale models should be preferred for their high reliability (Icardi *et al.* 2014; Crabill, Witherden & Jameson 2018), but have the inconvenience of being very expensive from a computational point of view, especially when one needs to characterize the flow with respect to variations of the pore properties. An alternative to expensive pore-scale simulations is the use of averaged models like the Darcy equation (Darcy 1856) or its Brinkman extension (Brinkman 1949). These models are computationally less expensive than their full-scale counterparts and allow one to find a solution that is equivalent to the full-scale solution in an averaged sense. However, one of their limitations resides in the presence of free parameters, such as the permeability, which depend on the microscopic properties of the structure. While these parameters were *a priori* unknown in the seminal work of Darcy, we are now able, because of multiscale techniques such as homogenization (Hornung 1997), to determine the values of the parameters from the solution of closure pore-scale problems. For this reason, homogenization provided relevant insights towards the modelling of multiscale fluid–structure interactions, extending the classical Darcy model to treat inertia within the pores (Zampogna & Bottaro 2016; Zampogna *et al.* 2016) and handling interfaces between porous and free-fluid regions (Lācis & Bagheri 2017; Lācis, Zampogna & Bagheri 2017; Lācis *et al.* 2020). In Zampogna & Gallaire (2020) homogenization revealed itself as a suitable tool to describe flows around inhomogeneous microstructured permeable surfaces or membranes, opening the path to a more formal approach in the characterization and design of membranes and filters.

The flow modifications induced by permeable membranes may find several applications. As mentioned above, the dandelion pappus, which can be modelled as a permeable membrane, shows values of drag coefficient larger than if the pappus was completely impervious (Cummins *et al.* 2018). Therefore, the modification of the permeability of a

membrane is a strategy to control and optimize the flow morphology. Lagrangian-based approaches are one category of optimization procedures, which have attracted much interest in the fluid dynamics community, and are based on a variational formulation that allows one to compute gradients at low cost through the use of the so-called adjoint variables (Luchini & Bottaro 2014). Several studies were developed in a Lagrangian framework, as in the case of the sensitivity to baseflow modifications (Marquet, Sipp & Jacquin 2008), steady forcing in the bulk (Boujo, Ehrenstein & Gallaire 2013; Meliga *et al.* 2014) or at solid walls by blowing and suction (Meliga, Sipp & Chomaz 2010; Boujo & Gallaire 2014, 2015), for different objectives and flow configurations. Adjoint-based sensitivity analysis tools can therefore be used as a building block for optimization procedures, in steady (Camarri & Iollo 2010) and unsteady (Nemili *et al.* 2011; Lemke, Reiss & Sesterhenn 2014) configurations. In Schulze & Sesterhenn (2013) an adjoint-based optimization procedure to obtain the optimal permeability distribution for trailing-edge noise reduction was proposed, in which the porous medium was modelled via the Darcy law.

Despite the increasing interest in multiscale structures in fluid mechanics, systematic approaches for the homogenization-based design and optimization of permeable membranes are still lacking. In the present work, we aim to bridge this gap by linking the obtained optimal profile of permeability to a real, realistic, full-scale structure (that can be eventually built). For this purpose, we propose a formal framework for the optimization of permeable membranes, applying it to the particular case of wake flows in the low- to moderate-Reynolds-number regime. We exploit the concepts of stability analysis, homogenization theory and gradient-based optimization so as to give a procedure to obtain the full-scale structure satisfying user-defined macroscopic flow objectives. The paper is structured as follows. In § 2, we introduce the mathematical formulation of the problem and describe the homogenization-based design procedure. We then apply the procedure by first studying, in § 3, the steady solutions of the flow equations and their linear stability with respect to infinitesimal perturbations. Section 4 is devoted to the geometric reconstruction of the microscopic geometry for salient cases and to the comparison with the homogenized model. In § 5, we then move to a gradient-based optimization of a membrane with variable properties, and in § 6, using a homogenization-based inverse procedure, we retrieve the full-scale geometry of the considered membrane from the optimal properties found in § 5 and eventually compare the properties of the full-scale structure with those predicted by the homogenized model.

2. A formal framework to support the design of microstructured permeable surfaces

In this section, we introduce the main physical hypotheses, strategy and tools to aid the design of microstructured membranes in order to tune their aerodynamic and hydrodynamic properties.

2.1. *Problem formulation and model description*

We consider a two-dimensional permeable cylindrical shell of diameter D subject to an incompressible flow of a Newtonian fluid of constant density ρ and viscosity μ, whose free-stream velocity is U, as depicted in figure 1. The cylindrical shell is constituted of a monodisperse repetition of solid inclusions, whose characteristic length scale is denoted as ℓ. Since $\ell \ll D$ we can introduce a separation-of-scales parameter defined as the ratio

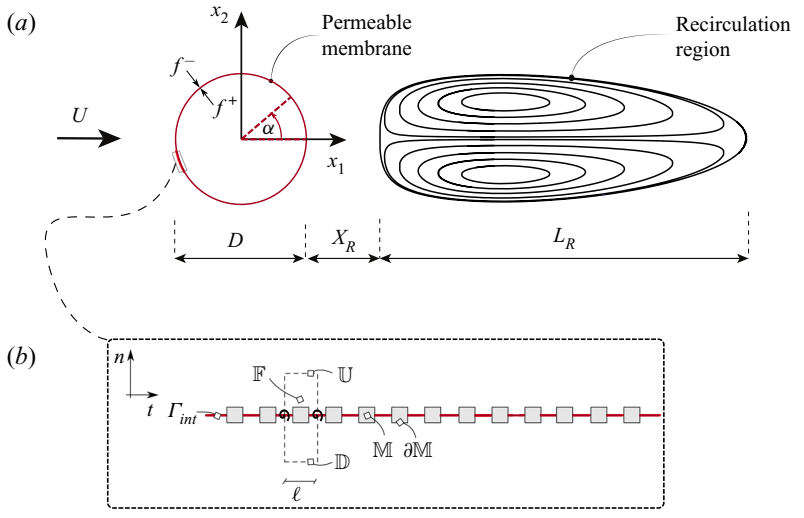

Figure 1. (*a*) Fluid flow configuration considered in the present work and its typical structure past the cylindrical permeable shell (Γ_{int}, in red) of diameter D, where we denote the length of the recirculation region L_R and its distance X_R from the rear of the body. The angle α is measured counterclockwise starting from the rear. The superscript minus sign indicates that the generic variable f is evaluated in the outer fluid region while the superscript plus sign refers to the inner fluid region. (*b*) Zoom on the shell to highlight its microscopic structure in cylindrical coordinates, made by replication of solid inclusions denoted by $\mathbb{M}$ with boundary $\partial\mathbb{M}$ and sketch of the elementary unit cell in dashed line, whose tangential-to-surface size is ℓ. The fluid domain within the unit cell is denoted by $\mathbb{F}$ while its upper and lower boundaries are indicated, respectively, with $\mathbb{U}$ and $\mathbb{D}$.

between the two length scales at play:

$$\varepsilon := \frac{\ell}{D} \ll 1. \tag{2.1}$$

Under this assumption, a homogenized model is employed to describe the flow through the membrane (Zampogna & Gallaire 2020), which is macroscopically represented by a smooth surface with zero thickness. In the outer and inner pure-fluid regions split by the permeable shell, the incompressible Navier–Stokes equations hold. The velocity $\boldsymbol{u}^*$ and pressure p^* fields are introduced, where the superscript * denotes dimensional variables. Introducing the Cartesian coordinate system (x_1, x_2) (figure 2), these equations read $(i, j = 1, 2)$

$$\left.\begin{gathered}\rho\partial_t^* u_i^* + \rho u_j^* \partial_j^* u_i^* = -\partial_i^* p^* + \mu\partial_{jj}^{*2} u_i^*, \\ \partial_i^* u_i^* = 0.\end{gathered}\right\} \tag{2.2}$$

The flow through the membrane is described by an effective stress jump model, consisting of the discontinuity in the fluid stress and the continuity of velocity across the permeable shell, denoted here with Γ_{int} (red line in figure 1). Labelling with the superscript $^-$ and $^+$ variables evaluated respectively in the outer and inner fluid regions, as shown in figure 1, the interface conditions at the membrane Γ_{int} read $(i, j, k = 1, 2)$

$$\left.\begin{gathered}u_i^* = u_i^{*+} = u_i^{*-}, \\ u_i^* = \frac{\ell}{\mu} M_{ij}\left(\Sigma_{jk}^*\left(p^{*-}, \boldsymbol{u}^{*-}\right) - \Sigma_{jk}^*\left(p^{*+}, \boldsymbol{u}^{*+}\right)\right) n_k,\end{gathered}\right\} \tag{2.3}$$

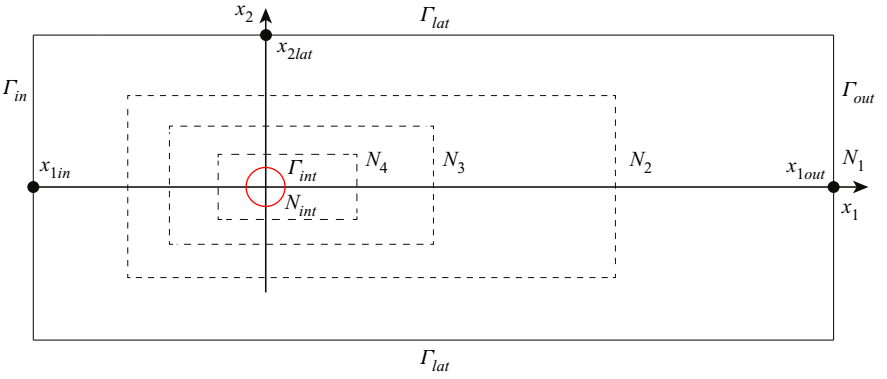

Figure 2. Computational domain considered in the present work. The regions denoted with N_j represent the different mesh refinements used when approaching the permeable shell. At the inlet Γ_{in} a free-stream condition with a Dirichlet boundary condition of the form $u_1^* = U$ and $u_2^* = 0$ is imposed, while on the lateral boundaries Γ_{lat} and at the oulet Γ_{out} the stress-free condition $(-p^*\delta_{ij} + \mu\partial_j^* u_i^*)n_j = 0$ is used. On the interface Γ_{int} conditions (2.3) are imposed.

where Σ_{jk}^* is the jkth component of the stress tensor defined as

$$\Sigma_{jk}^*\left(p^*, \boldsymbol{u}^*\right) = -p^*\delta_{jk} + \mu(\partial_j^* u_k^* + \partial_k^* u_j^*), \tag{2.4}$$

and the components of the tensor M_{ij} (figure 1) are

$$M_{ij} = \bar{L}_t t_i t_j - \bar{F}_n n_i n_j, \tag{2.5}$$

where $\bar{L}_t$, $\bar{F}_n$ are evaluated by solving microscopic problems within the elementary unit cell introduced in figure 1, in the local reference frame $(\boldsymbol{t}, \boldsymbol{n}) = ((-\sin(\alpha), \cos(\alpha)), (\cos(\alpha), \sin(\alpha)))$ (see Zampogna & Gallaire (2020) and § 4.2 for a detailed description of these problems and their solution). We note that the generic tensor N_{ij} of the original condition developed in Zampogna & Gallaire (2020) is replaced here by $-M_{ij}$ since, in the present work, we consider only solid inclusions which are symmetric with respect to Γ_{int} and we assume that inertia is negligible within the pores.

By considering D and U respectively as reference length and velocity scales, we obtain the following system of non-dimensional equations:

$$\left.\begin{aligned} \partial_t u_i + u_j\partial_j u_i = -\partial_i p + \frac{1}{Re}\partial_{jj}^2 u_i, \\ \partial_i u_i = 0, \end{aligned}\right\} \tag{2.6}$$

where we introduce the Reynolds number as $Re = \rho UD/\mu$. The non-dimensional interface condition on Γ_{int} reads

$$\left.\begin{aligned} u_i = u_i^+ = u_i^-, \\ u_i = Re\mathcal{M}_{ij}\left(\Sigma_{jk}\left(p^-, \boldsymbol{u}^-\right) - \Sigma_{jk}\left(p^+, \boldsymbol{u}^+\right)\right)n_k, \end{aligned}\right\} \tag{2.7}$$

$$\Sigma_{jk}(p, \boldsymbol{u}) = -p\delta_{jk} + \frac{1}{Re}(\partial_j u_k + \partial_k u_j), \tag{2.8}$$

$$\mathcal{M}_{ij} = \mathcal{L}t_i t_j - \mathcal{F}n_i n_j, \tag{2.9}$$

where $\mathcal{L} = \epsilon\bar{L}_t$ and $\mathcal{F} = \epsilon\bar{F}_n$ are respectively labelled as slip and filtrability numbers. The interface condition (2.7) thus states that the velocity at the membrane is proportional

to the Reynolds number and to the tensor $\mathcal{M}_{ij}$. According to Zampogna & Gallaire (2020), the tensor $\mathcal{M}_{ij}$ describes the geometry of the microscopic problem with negligible inertial effects within the microscopic domain, in a non-dimensionalization which makes the problem independent of the macroscopic Reynolds number. In the macroscopic perspective, the relative importance between inertial and viscous effects is taken into account by Re in (2.7). More specifically, the velocity locally tangential to the interface is proportional to $\mathcal{L}$, while the normal velocity is proportional to $\mathcal{F}$. Therefore, the filtrability and slip numbers denote the capability of the flow to pass through and slip along the membrane, respectively. Different limiting behaviours of the interface condition (2.7) are thus identified. When $\mathcal{F} = 0$, the flow cannot pass through the membrane but it can slip along it. This situation is analogous to the one outlined in Zampogna, Magnaudet & Bottaro (2019) for rough surfaces, and the resulting boundary condition is formally analogous to the so-called Navier slip condition. When $\mathcal{L} = 0$, a no-slip condition is imposed on the tangential velocity, while the normal one varies in proportion to $\mathcal{F}$. This situation can be interpreted as an averaged Darcy law through the membrane, where the viscous effects and thus the slip at the interface are neglected (Zampogna & Bottaro 2016). Other limiting cases occur for $\mathcal{F} = 0$ and $\mathcal{L} = 0$, which corresponds to a solid wall condition, and for $\mathcal{F} \to \infty$ and $\mathcal{L} \to \infty$, which corresponds to the imposition of the continuity of stresses across the microscopic elementary volume whose size tends to zero, and thus to the absence of the solid structure. Since the flow configuration is solved numerically, we refer to the caption of figure 2 for an explanation of the boundary conditions imposed on the remaining boundaries of the computational domain. These conditions, in non-dimensional form, read $u_1 = 1$, $u_2 = 0$ at the inlet and $(-p\delta_{ij} + (1/Re)\partial_j u_i)n_j = 0$ on the lateral and outlet boundaries.

2.2. *Homogenization-based design*

In the existing literature, works on permeable bodies and membranes were focused on the evaluation of the macroscopic parameters of the membrane (slip and filtrability) starting from the microscopic geometry. Other works treated the above-mentioned macroscopic quantities as free parameters in order to characterize, modify and optimize the fluid flow surrounding the porous body, without providing an explicit link between these parameters and the microscopic structure of the membrane. Here, we propose to fill the gap between these two aspects by an inverse formulation of the homogenized model that, on the one hand, is extremely efficient for parametric studies and, on the other hand, allows one to deduce the microscopic geometry which realizes given distributions of $\mathcal{L}$ and $\mathcal{F}$.

The inverse formulation aims at deriving the microscopic characteristics of the membrane based on the macroscopic features of the steady flow. In the present paper, an efficient workflow for deducing full-scale structures starting from the homogenized model is adopted (cf. the top frame of figure 3). The generic workflow therefore firstly consists of an analysis where the homogenized model is employed. The implementation of the homogenized model implies a decoupling between the microscopic structure and the macroscopic effect on the flow. On the one hand, parametric studies and optimizations are simplified owing to the reduced number of parameters; on the other hand, the retrieval of the full-scale structure is performed in a second step, when the macroscopic feedback embodied in the scalar parameters of the homogenized model is already known.

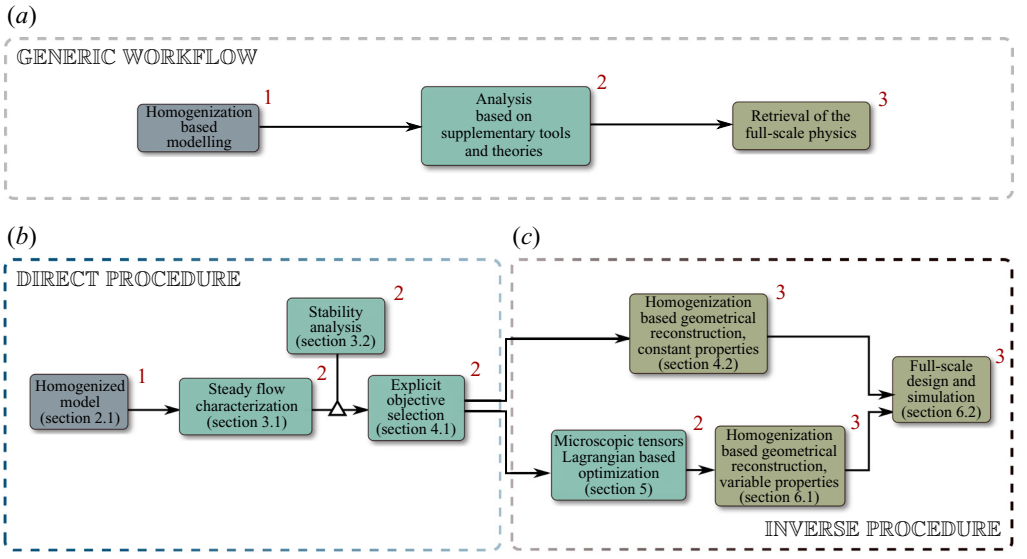

Figure 3. (*a*) Generic workflow to efficiently analyse a flow configuration via homogenized models integrated in classical analyses like, for instance, parametric studies, stability analysis or adjoint-optimization finalized to identify configurations of interest. The retrieval of the full-scale physics for the identified configurations is done in a last step leading to a substantial reduction of the complexity of the optimization problem. (*b*,*c*) The generic workflow has been specialized in the present paper for the design of permeable membranes. Colours and red numbers are used to correctly place each step of the procedure adopted in the present paper in the generic workflow. A homogenized model is used to characterize a specific flow configuration in a direct formulation. This allows one to identify a set of objectives and the corresponding values of the macroscopic parameters realizing these objectives. Homogenization is then used in an inverse formulation to associate the values of the macroscopic tensors with a specific microscopic geometry.

For illustration purposes, the workflow is specialized to analyse the flow configuration shown in figure 1, leading to the following procedure:

(i) Using the homogenized approach described in the previous section, we perform a parametric study for varying $\mathcal{L}$ and $\mathcal{F}$, by solving the steady version of (2.6)–(2.7) for different values of the Reynolds number.

(ii) We characterize the topological properties of the steady flow (e.g. the characteristic dimensions of the recirculation region) and the aerodynamic/hydrodynamic properties of the permeable shell, such as its drag coefficient.

(iii) The validity of the performed investigation, carried out assuming that the flow is steady, is verified by linear stability analysis (Chomaz 2005; Theofilis 2011). The latter has the advantage of characterizing the stability of the steady solution with a computational cost comparable with that needed to compute steady solutions, thus making it suitable for the performed parametric study.

(iv) Once the variety of possible steady solutions is reduced by excluding the unstable configurations, for which the steady analysis would be inappropriate, the objective to be optimized is defined, e.g. the maximum drag coefficient for a fixed Reynolds number. Therefore, the values of $\mathcal{L}$ and $\mathcal{F}$ that maximize the objective function are identified. This can be done by employing adjoint procedures for spatially homogeneous membrane properties. However, since in this work we perform a parametric study, the values are directly deduced from the latter.

(v) We then move from the macroscopic perspective to the microscopic one, aiming at identifying the geometry of the membrane that corresponds in macroscopic terms to the optimal configuration previously identified. We therefore perform the microscopic simulations described in Zampogna & Gallaire (2020) for a fixed geometry by varying the fluid-to-solid ratio of the porous shell. We thus define the microscopic geometrical parameters and ε.

(vi) We eventually verify the accuracy of the resulting structure by comparing the full-scale simulations with the homogenized results.

The outlined technique has the great advantage of markedly reducing the complexity of the problem and giving a parametric map of the properties of the flow by varying the microscopic geometry of the membrane. An extension of this technique to treat the case of a microscopic geometry that varies along the membrane is obtained by a gradient-based optimization implemented via a Lagrangian approach, detailed in § 5.2. In particular, we consider as a starting point the configuration, with constant slip and filtrability numbers, that maximizes the drag coefficient. We evaluate the sensitivity of this predefined objective function (drag maximization) with respect to spatial inhomogeneities of the properties of the membrane and perform a gradient-based optimization. The resulting structure is then obtained by following an inverse procedure based on the microscopic calculations of Zampogna & Gallaire (2020), but extended to the case of variable properties along the membrane.

We finally underline that the procedure, illustrated here for the specific case of a wake flow, is of general validity and can thus be applied to a generic flow.

3. Case study: flow past a cylindrical porous shell

In this section, we report the results of the direct part of the procedure sketched in figure 3, preparatory to the homogenization-based geometrical reconstruction and Lagrangian optimization, constituting the inverse part of the procedure. We characterize the steady flow in terms of the recirculation region and drag coefficient, and then we move to the stability properties of the steady wake and the features of possible unsteady modes.

Equations (2.6) are numerically implemented via their weak formulation in the finite-element solver COMSOL Multiphysics, using a domain decomposition method (e.g. Quarteroni 2017) to couple the outer and inner flows. In this framework, the macroscopic model (2.7) acts like an interface condition between two different fluid domains. In order to exchange information from the outer to the inner domain, the stress jump condition is implemented by exploiting the interface integral emerging from the weak formulation, while, to exchange information from the inner to the outer domain, the continuity of velocity is imposed via a Dirichlet boundary condition. We exploit the built-in solver for nonlinear systems, based on a Newton algorithm. The spatial discretization is based on the Taylor–Hood (P2-P1) triangular elements. The unstructured grid is made of five different regions of refinement (figure 2), whose edge densities have been chosen after a convergence analysis reported in Appendix A.

The eigenvalue problems resulting from the linear stability analysis carried out in § 3.2 are solved with the COMSOL Multiphysics built-in eigenvalue solver, based on the ARPACK library; mesh convergence is checked also for this problem and it is reported in Appendix A.

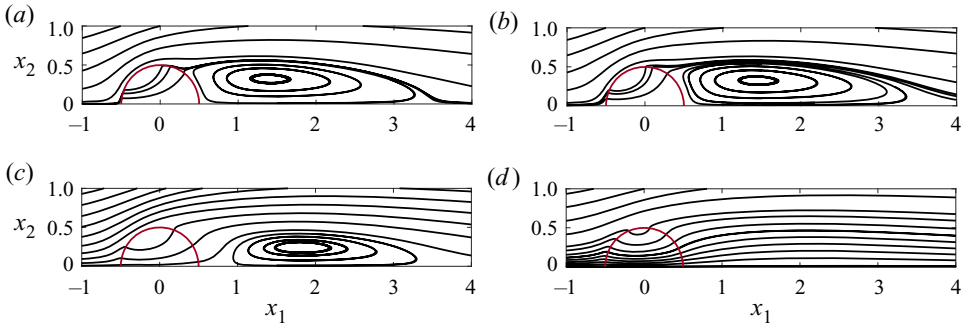

Figure 4. Streamlines of the flow past the cylindrical permeable shell at $Re = 50$ for $\mathcal{L} = 10^{-4}$ and four different values of $\mathcal{F}$: (*a*) $\mathcal{F} = 10^{-4}$, (*b*) $\mathcal{F} = 10^{-3}$, (*c*) $\mathcal{F} = 10^{-2}$ and (*d*) $\mathcal{F} = 3 \times 10^{-2}$.

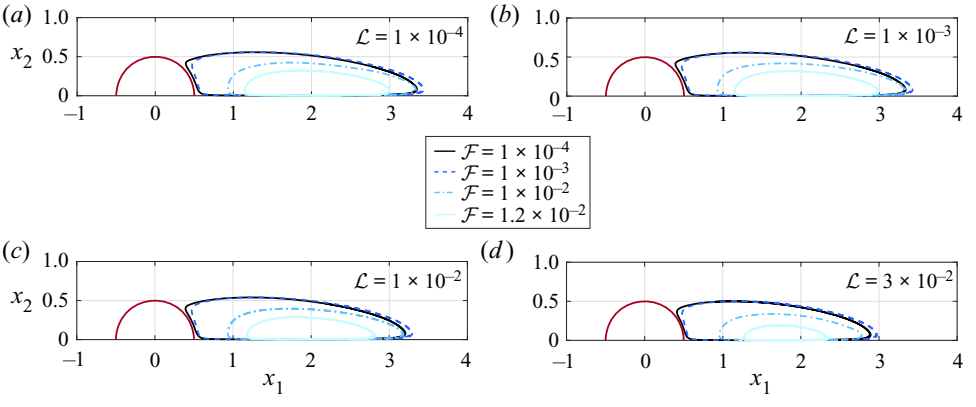

Figure 5. (*a–d*) Streamlines identifying the recirculation region past the cylindrical permeable shell at $Re = 50$ for different values of $\mathcal{F}$. Each panel corresponds to a single value of $\mathcal{L}$.

3.1. *Steady flow characterization*

The steady wake past a circular solid cylinder is characterized by a recirculation region that is symmetric with respect to the x_1 axis. We denote with $(\boldsymbol{U}, P)$ the steady solution of (2.6). Since, by construction, we do not introduce any further asymmetry, also the flow past the permeable cylindrical shell is expected to be x_1-symmetric. For this reason, we only report the flow field in the region $x_2 > 0$. For the present analysis, we introduce the length of the recirculation region L_R and its distance from the rear of the body X_R as defined in figure 1. In figure 4 we report the flow streamlines for different values of $\mathcal{F}$ when $Re = 50$ and $\mathcal{L} = 10^{-4}$. At low values of $\mathcal{F}$, e.g. $\mathcal{F} = 10^{-4}$, the wake is similar to the solid case, i.e. characterized by a recirculation region attached to the rear of the cylinder ($X_R \approx 0$). As the value of $\mathcal{F}$ increases, the recirculation region detaches from the body and moves downstream. A further increase in $\mathcal{F}$ implies a size reduction of the recirculation region (L_R), and at very large values of $\mathcal{F}$, i.e. $\mathcal{F} = 3 \times 10^{-2}$, the recirculation region eventually disappears ($L_R = 0$).

In figure 5 we report the variation of the recirculation region with $\mathcal{F}$, for different slip numbers $\mathcal{L}$ and for $Re = 50$. Independently of the value of the slip number, a behaviour similar to that described in figure 4 is observed. For a fixed filtrability number, an increase in $\mathcal{L}$ leads to a slight decrease of L_R, while X_R does not vary noticeably.

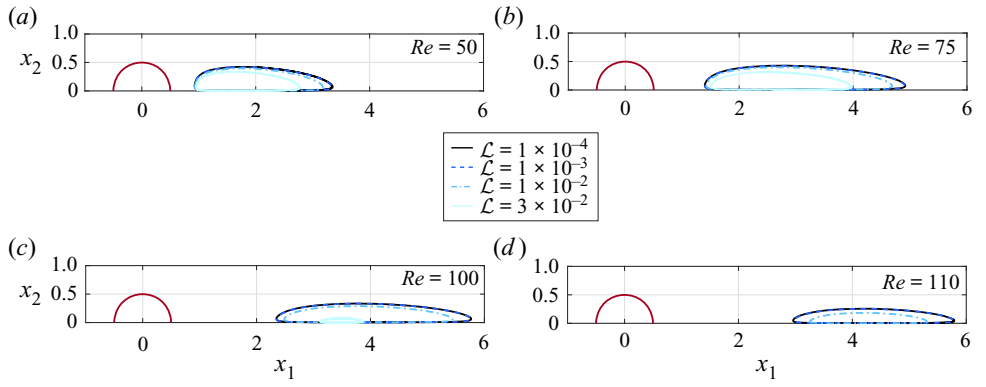

Figure 6. (*a–d*) Streamlines identifying the recirculation region past the cylindrical permeable shell at $\mathcal{F} = 10^{-2}$ and for different values of Re and $\mathcal{L}$. Note that for $\mathcal{L} = 3 \times 10^{-2}$ and $Re = 110$, recirculation is suppressed.

A complete characterization of the flow morphology requires also the analysis of the effect of the Reynolds number. In figure 6 we show the recirculation regions for fixed filtrability number $\mathcal{F} = 10^{-2}$, for different values of $\mathcal{L}$ and for $Re = 50$, 75, 100 and 110. For $Re = 50$, the flow is characterized by a recirculation detached from the body such that $L_R \approx 2$. At $Re = 75$, the recirculation region moves downstream and L_R increases. This effect is enhanced at large values of the slip number. In the last case, $Re = 110$, the recirculation region moves further downstream and L_R decreases, and eventually disappears for large values of $\mathcal{L}$.

The evolution of L_R and X_R with $\mathcal{L}$, $\mathcal{F}$ and Re is summarized in figure 7. The quantities L_R and X_R have been deduced by a Matlab script which evaluates the position of the zeros of the horizontal velocity field sampled on the line $x_2 = 0$. In analogy with the solid case, L_R increases with Re (figure 7*a*). The curves are grouped in clusters. Each cluster represents different values of Re, and each curve within the cluster a different value of $\mathcal{L}$. For $Re = 25$, L_R decreases with $\mathcal{F}$ until the recirculation region disappears for $\mathcal{F} \approx 10^{-2}$. A similar trend is observed for $Re = 50$, but in this case the recirculation region disappears for larger values of $\mathcal{F}$. For $Re > 50$, interestingly, the recirculation region grows as the filtrability number increases. The value of L_R reaches a maximum and decreases, until the recirculation region disappears for $\mathcal{F} \approx 1.5 \times 10^{-2}$. For all cases, an increase in $\mathcal{L}$ leads to a slight decrease of L_R, while the trend with $\mathcal{F}$ does not change.

As shown in figure 7(*b*), the distance between the body and the recirculation region, X_R, increases with $\mathcal{F}$, reaching a maximum value approximately equal to 2 for $Re = 100$, while the effect of $\mathcal{L}$ is negligible. An increase in Re leads to an increase in the distance X_R, but the trend with $\mathcal{F}$ remains unchanged.

The morphology analysis of the steady wake shows that L_R and X_R are controlled by the slip and filtrability numbers. Large values of the filtrability number $\mathcal{F}$ strongly influence the flow, implying detached and small recirculation regions, or even the absence of recirculation. The slip number $\mathcal{L}$ slightly modifies the shape and distance of the recirculation region, for fixed filtrability number, whilst the qualitative behaviour remains unchanged. An increase in the Reynolds number, for large values of $\mathcal{F}$, leads to an initial increase in L_R, followed by a decrease and eventually vanishing, while X_R monotonically increases. The outlined wake morphology strongly resembles that observed for the wake

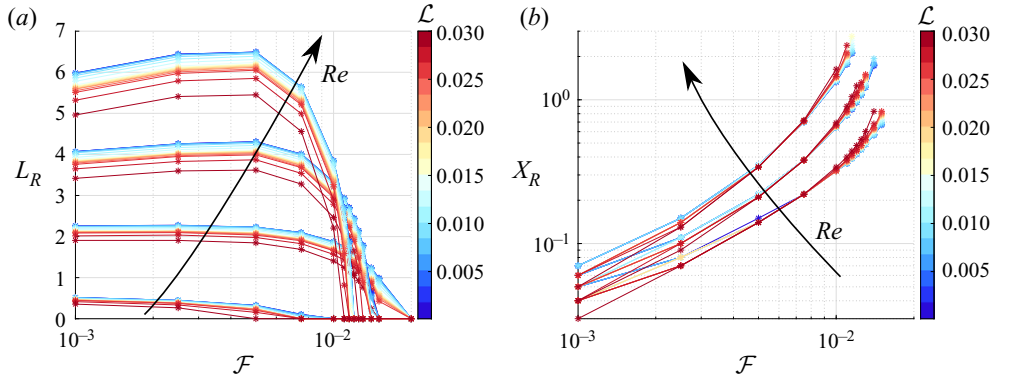

Figure 7. (*a*) Length of the recirculation region past the cylindrical permeable shell L_R for $\mathcal{F} \in [10^{-3}, 2 \times 10^{-2}]$ and $\mathcal{L} \in [10^{-3}, 2 \times 10^{-2}]$. Each cluster represents a single value of Re. From top to bottom: $Re = 100, 75, 50, 25$. (*b*) Distance of the recirculation region from the rear of the body X_R for the same values of the parameters. From bottom to top: $Re = 50, 75, 100$.

of porous rectangles (Ledda *et al.* 2018), where the permeability plays a role similar to that of the filtrability number.

When the Reynolds number increases, the inertia of the fluid increases and tends to enlarge the recirculation region, whereas the flow can pass through the body more easily, since the velocity at the membrane is proportional to Re (equation (2.7)). The result of this competition is the non-monotonic behaviour of the recirculation region size with Re.

We conclude our characterization of the steady wake past a permeable cylindrical shell by considering the drag coefficient:

$$C_D = 2 \oint_{\Gamma_{cyl}} \left(\Sigma_{jk}\left(P^-, \boldsymbol{U}^-\right) - \Sigma_{jk}\left(P^+, \boldsymbol{U}^+\right) \right) n_k \delta_{1j} \, \mathrm{d}\Gamma, \tag{3.1}$$

i.e. the drag exerted by the fluid over the outer ($^-$) and inner ($^+$) sides of Γ_{int}. The drag coefficient of a solid cylinder decreases with Re (Fornberg 1980). The same behaviour is observed in the permeable case (cf. figure 8), where, at each value of Re, we observe clusters of curves analogous to figure 7. While $\mathcal{L}$ produces slight variations in C_D, the trend in the variation with $\mathcal{F}$ depends on the Reynolds number considered and shows two different types of behaviour. Up to $Re = 15$, the drag coefficient decreases with $\mathcal{F}$. From $Re = 20$, C_D slightly increases with $\mathcal{F}$, and this effect is more pronounced as Re further increases. For larger values of Re, the curve representing C_D against $\mathcal{F}$ is no longer monotonic and for $Re = 100$, a clear peak is observed, for $\mathcal{F} \approx 1.25 \times 10^{-2}$. Surprisingly, the maximum drag coefficient $C_D \approx 1.34$ is larger than that for the solid cylinder, $C_D \approx 1.06$ (Fornberg 1980). Beyond this value of $\mathcal{F}$, the drag coefficient decreases.

In the following, a physical insight into the described drag behaviour is provided. Since the maximum is observed by varying the filtrability, while the slip does not have any significant effect on this behaviour, we fix $\mathcal{L} = 10^{-4}$ and we focus on the effect of solely $\mathcal{F}$ in the range $[10^{-4}, 5 \times 10^{-2}]$, for $Re = 100$. Note that the maximum of the drag coefficient in this specific case is obtained for $\mathcal{F} \simeq 1.2 \times 10^{-2}$, which is inside the range considered here. We perform an analysis of the different sources of drag, dividing them into a pressure contribution, i.e. $(\Delta P)n_1 = -(P^- - P^+)n_1$, and a viscous stress contribution $(\Delta \Sigma^v_{1j})n_j = (\Sigma^v_{1j}(\boldsymbol{U}^-) - \Sigma^v_{1j}(\boldsymbol{U}^+))n_j$, where $\Sigma^v_{jk}(\boldsymbol{U}) = (1/Re)(\partial_j U_k + \partial_k U_j)$. These contributions are reported in figure 9(*a*,*b*). The global pressure and viscous contributions to the drag are

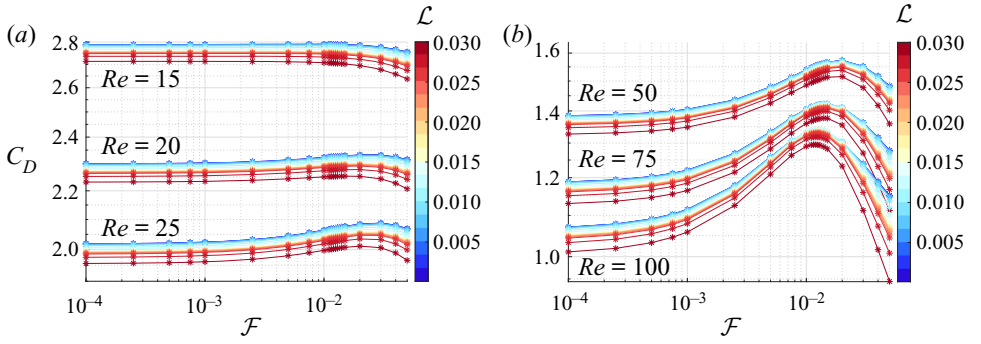

Figure 8. (*a*,*b*) Variation of the drag coefficient C_D with $\mathcal{F}$ for different values of $\mathcal{L}$. Each cluster corresponds to a different value of *Re*, as denoted in the figure.

the integrals of the corresponding curves in figure 9(*a*,*b*). Analysing the integral of the pressure and viscous contributions we observe that (i) the viscous contribution is approximately ten times smaller than the pressure one (except for the case $\mathcal{F} = 5 \times 10^{-2}$) and (ii) the viscous contribution increases with $\mathcal{F}$, while the pressure contribution has a maximum at $5 \times 10^{-3} < \mathcal{F} < 10^{-2}$. As a result, the non-monotonic behaviour of C_D versus $\mathcal{F}$ can be largely explained by investigating the sole pressure contribution. In the almost-solid case, $\mathcal{F} = 10^{-4}$ (blue line), there is no fluid motion inside the cylinder, and the inner pressure is constant, as shown in figure 9(*c*). Therefore, the inner pressure does not contribute to the drag and the distribution of external pressure is alone responsible for integral forces. Focusing on the upper half of the cylinder ($x_2 > 0$), in the front part, for $(3/4)\pi < \alpha < \pi$, the pressure contribution is positive and becomes negative for $\pi/2 < \alpha < (3/4)\pi$. This suction region reduces the total drag since it acts on the front part of the cylinder. In the rear of the cylinder, the pressure contribution is positive with an almost constant negative value, which is the so-called base region. As the filtrability increases, a fluid motion manifests in the inner region of the cylinder, which is associated with a non-uniform distribution of inner pressure (see figure 9*d*). The pressure difference in the upstream part of the cylinder decreases as the filtrability increases since the membrane is progressively more permeable. Thus, an inner flow, oriented towards the downstream face of the cylinder, is generated. As a result of the blockage represented by the downstream cylinder face for the inner flow, the inner pressure increases moving downstream, as indicated by the concavity of the streamlines (see figure 9*c*–*e*). At the same time, the external base pressure in the downstream surface of the cylinder is not significantly affected by $\mathcal{F}$ provided that $\mathcal{F} < 10^{-2}$. As a result, the contribution to drag of the pressure difference in the downstream face of the cylinder is larger than for the solid case for $\mathcal{F} < 10^{-2}$. Figure 9(*a*,*b*) supports this discussion from a quantitative viewpoint. In particular, comparing cases with $\mathcal{F} < 10^{-2}$ it is possible to see that, as $\mathcal{F}$ increases, (i) the suction at $\alpha \simeq (3/4)\pi$ decreases (thus increasing the drag), (ii) the drag contribution of the upstream face decreases and (iii) the drag contribution of the downstream face increases. At low filtrabilities, (i) and (iii) dominate over (ii), while at larger values of $\mathcal{F}$ the term (ii) becomes predominant. Concerning the viscous contribution, although more modest, figure 9(*a*,*b*) shows that it monotonically increases with $\mathcal{F}$.

Conversely, as $\mathcal{F}$ is further increased, see the case $\mathcal{F} = 5 \times 10^{-2}$, the upstream contribution markedly decreases due to the larger filtrability of the membrane. The substantially higher velocities of the inner flow and the larger filtrability cause a very mild

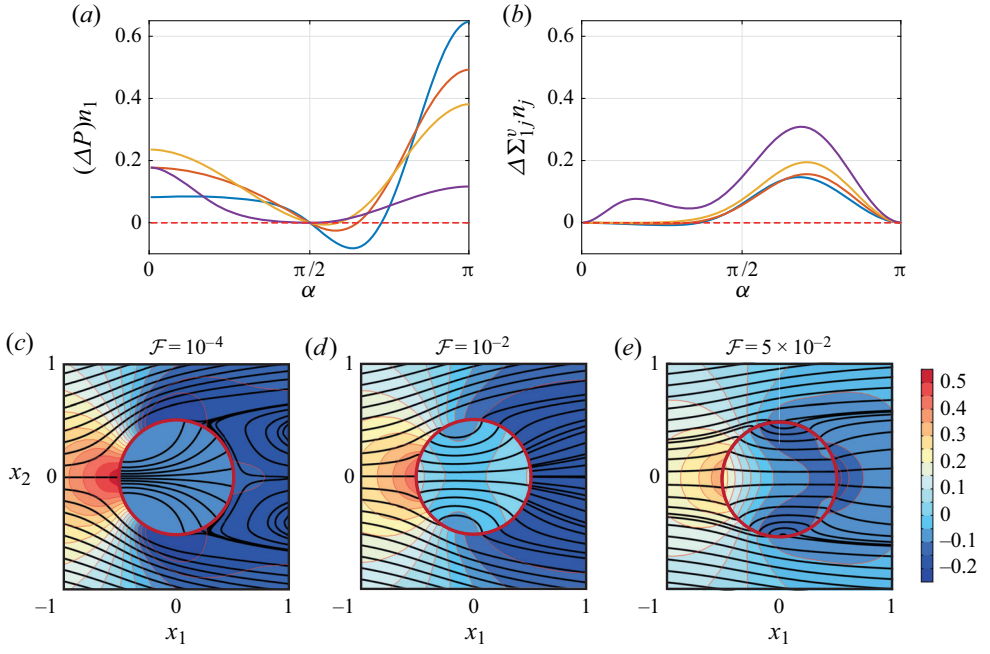

Figure 9. Pressure (*a*) and viscous stress (*b*) contributions to the drag following the cylinder surface. The angle α is measured counterclockwise starting from the rear. The colours denote different values of $\mathcal{F} = 10^{-4}$ (blue), $\mathcal{F} = 5 \times 10^{-3}$ (orange), $\mathcal{F} = 10^{-2}$ (yellow), $\mathcal{F} = 5 \times 10^{-2}$ (purple). The slip number is kept fixed to $\mathcal{L} = 10^{-4}$. (*c*)–(*e*) Streamlines (black bold lines) and iso-contours of the pressure for the steady flow around and through the permeable circular membrane, for different values of $\mathcal{F}$ and $\mathcal{L} = 10^{-4}$.

increase of the inner pressure when approaching the downstream part of the membrane. This is again shown also by the streamlines (see figure 9*e*) which are almost straight in the inner region. Moreover, the larger flow across the downstream part of the membrane decreases the pressure jump between external and internal flows in that area. As a net result, the pressure contribution to drag, in comparison with the impermeable case (here approximated by $\mathcal{F} = 10^{-4}$) decreases also in the downstream region. Although the viscous contribution to the drag increases, the total drag decreases because it is quantitatively dominated by the pressure, whose contribution rapidly decays.

In this section, we characterized the morphology of the steady flow, describing the effect of the slip and filtrability numbers. However, not all steady solutions previously described can be observed, as some of them may be unstable with respect to perturbations, thus leading to unsteady configurations. Since conducting time-dependent simulations for every studied case (far beyond 1000) is a monumental task, we perform a stability analysis, well known to give very accurate predictions of the bifurcations for the case at issue in computational times comparable with the ones of the steady analyses (Chomaz 2005; Theofilis 2011). Thus, in the following we study the stability of the steady-flow solution as $\mathcal{L}$ and $\mathcal{F}$ are varied.

3.2. *Stability analysis of the steady flow*

As mentioned in the previous section, to complete the analysis of the chosen flow configuration, we now establish for which combinations of $(Re, \mathcal{F}, \mathcal{L})$ the solution is

linearly stable with respect to perturbations and thus likely to be observed. The occurrence of bifurcations of the flow leading to different configurations is studied in the framework of linear stability analysis (Chomaz 2005; Theofilis 2011). We consider the flow solution as the superposition of the steady solution denoted as $[\boldsymbol{U}(x, y), P(x, y)]$, outlined in the previous section, and an infinitesimal unsteady perturbation. We thus introduce the following normal mode ansatz:

$$u_i(x, y, t) = U_i(x, y) + \sigma \hat{u}_i(x, y) \exp(\lambda t), \quad p(x, y, t) = P(x, y) + \sigma \hat{p}(x, y) \exp(\lambda t), \tag{3.2a,b}$$

where $\sigma \ll 1$. At $O(1)$ the steady version of the flow equations is obtained, satisfied by $[\boldsymbol{U}, P]$, and at $O(\sigma)$ the following system of equations is obtained:

$$\left.\begin{gathered} \lambda \hat{u}_i + \hat{u}_j \partial_j U_i + U_j \partial_j \hat{u}_i = -\partial_i \hat{p} + \frac{1}{Re} \partial^2_{jj} \hat{u}_i, \\ \partial_i \hat{u}_i = 0, \end{gathered}\right\} \tag{3.3}$$

$$\left.\begin{gathered} \hat{u}_i = \hat{u}_i^+ = \hat{u}_i^-, \\ \hat{u}_i = Re \mathcal{M}_{ij} \left(\Sigma_{jk} \left(\hat{p}^-, \hat{\boldsymbol{u}}^- \right) - \Sigma_{jk} \left(\hat{p}^+, \hat{\boldsymbol{u}}^+ \right) \right) n_k, \end{gathered}\right\} \tag{3.4}$$

together with the homogeneous Dirichlet boundary condition at the inlet Γ_{in}, $\hat{u}_1 = \hat{u}_2 = 0$, and the stress-free condition on the sides Γ_{lat} and at the outlet Γ_{out}, $(-\hat{p}\delta_{ij} + (1/Re)\partial_j \hat{u}_i) n_j = 0$.

Equations (3.3) and (3.4), together with the boundary conditions on Γ_{in}, Γ_{lat} and Γ_{out}, define an eigenfunction problem with, possibly, complex eigenvalues $\lambda = \mathrm{Re}(\lambda) + \mathrm{i}\,\mathrm{Im}(\lambda)$. The real part of the eigenvalue is the growth rate of the global mode, and the imaginary part its angular velocity. We introduce the associated Strouhal number defined as $St = \mathrm{Im}(\lambda)/2\pi$. The flow is asymptotically unstable if there exists at least one eigenvalue with positive real part; otherwise it is asymptotically stable. The absence of unstable modes therefore ensures the occurrence of the steady solution, while their presence gives useful information about the emerging unsteady flow configuration.

We turn now to describe the results of the linear stability analysis. The solid case exhibits a Hopf bifurcation at $Re = 46.7$ that drives the flow to a state that is periodic in time, characterized by the alternate shedding of vortices, the so-called von Kármán vortex street (Barkley 2006). Ledda *et al.* (2018) showed the suppression of this vortex shedding mode for large enough values of the permeability, in the case of porous rectangular cylinders. A preliminary analysis of the permeable membrane shows that the above-described mode is also the only one that destabilizes the steady wake in the range $10 < Re < 130$. In figure 10 we report the marginal stability curves (i.e. the locus of points with $\mathrm{Re}(\lambda) = 0$) in the $(\mathcal{F}, Re)$ plane, for different values of $\mathcal{L}$. The marginal stability curves define a stable and an unstable region in the $(\mathcal{F}, Re)$ plane. At low values of $\mathcal{F}$ and $\mathcal{L}$, the critical Reynolds number Re_{cr} for the marginal stability coincides with the solid one, i.e. $Re_{cr} = 46.7$. An increase in $\mathcal{L}$ leads to a slight increase in Re_{cr} that reaches a maximum approximately equal to 50 for $\mathcal{L} = 0.02$. For $\mathcal{F} > 10^{-3}$ the critical Reynolds number increases. We identify a critical value of $\mathcal{F} = \mathcal{F}_{cr}$ beyond which the steady solution is stable. This value depends on the Reynolds and slip numbers. For fixed $\mathcal{L}$, $\mathcal{F}_{cr}$ initially increases with Re, reaches a maximum and decreases. Among all cases, the maximum value $\mathcal{F}_{cr} \approx 1.08 \times 10^{-2}$ is achieved for $\mathcal{L} \approx 10^{-4}$.

The imaginary part of the eigenvalue well approximates the oscillation frequency of the nonlinear limit cycle in marginal stability conditions (Barkley 2006). In the inset of

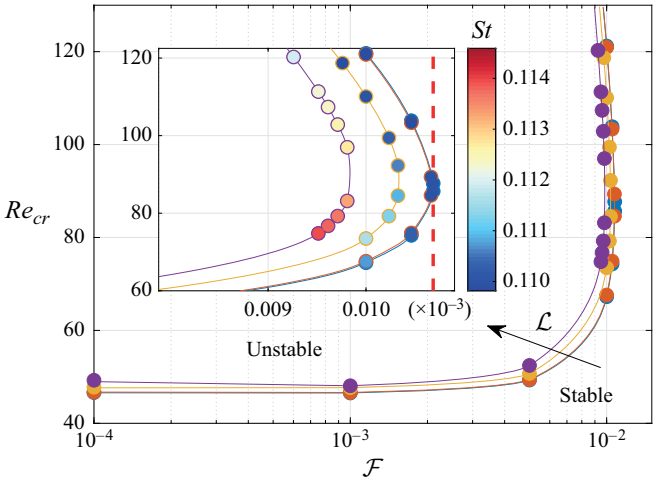

Figure 10. Marginal stability curves in the plane $(\mathcal{F}, Re)$. Each curve is associated with a different value of slip number $\mathcal{L} = 10^{-4}$ (blue), $\mathcal{L} = 10^{-3}$ (orange), $\mathcal{L} = 10^{-2}$ (yellow), $\mathcal{L} = 2 \times 10^{-2}$ (purple). The inset shows a zoom in for large values of $\mathcal{F}$. The coloured circles represent the values of the Strouhal number along the marginal stability curve in the region depicted in the inset.

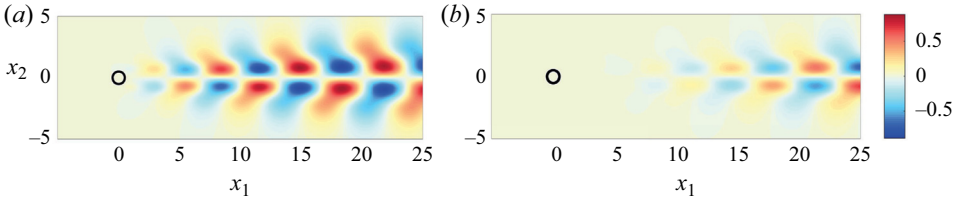

Figure 11. Real part of the eigenvector $\hat{u}_1$ associated with the marginally stable eigenvalue for $Re = 46.7$, $\mathcal{L} = 10^{-2}$ and $\mathcal{F} = 10^{-3}$ (a) and for $Re = 87$, $\mathcal{L} = 10^{-4}$ and $\mathcal{F} = 1.075 \times 10^{-2}$ (b). The velocity eigenvectors are normalized by their L_2 norm.

figure 10, we report the value of the Strouhal number along the marginal stability curve. We do not observe substantial variations in the Strouhal number with respect to the solid case, i.e. $St \approx 0.116$ (Norberg 2003).

In figure 11 we report the spatial distribution of $\mathrm{Re}(\hat{u}_1)$ for two different cases, in figure 11(a) characterized by a recirculation region close to the cylinder and in figure 11(b) characterized by a recirculation region far downstream. In both cases, the unstable mode leads to a vortex shedding similar to that of the solid case, as already anticipated. As the recirculation region moves downstream, the onset of the vortex shedding is displaced downstream and the flow in proximity of the cylinder is almost steady.

The analysis of the stability properties of the steady wake shows the strong stabilization effect of the filtrability number. The marginal stability curves strongly resemble those outlined in Ledda *et al.* (2018, 2019). In particular, the vortex shedding is suppressed for large enough values of the filtrability. This similarity is confirmed by the spatial distribution of the unstable mode, which moves downstream with the recirculation region of the steady flow. Indeed, the stability properties of the wake can be related to the extent of the so-called absolute region of instability in a local stability analysis (i.e. performed for the velocity profile at each streamwise location; see Monkewitz (1988) and Giannetti &

Luchini (2007)) that roughly corresponds to the recirculation region. As shown in Ledda *et al.* (2018), there is a critical value of the extent of the recirculation region beyond which the flow becomes unstable. When large values of the filtrability are considered, the recirculation region is small or even absent, and thus the vortex shedding is suppressed. For fixed $\mathcal{F} \approx 10^{-2}$ and $\mathcal{L}$ and increasing Re, the recirculation region initially increases and then decreases its dimensions (cf. figure 6). Therefore, the first destabilization and subsequent stabilization for fixed $\mathcal{F}$ and $\mathcal{L}$ are due to the non-monotonic behaviour of the length of the recirculation region with Re, which crosses the critical value for the marginal stability twice.

By comparing the marginal stability curve with the drag coefficient, we deduce that the maximum of C_D for the steady flow occurs for a stable configuration for all values of Re. Interestingly, a permeable circular membrane exhibits a larger drag than the equivalent solid one, and this maximum occurs when the steady flow is stable.

In the present section, we performed a parametric study under the framework of bifurcation theory in order to exclude the unstable configurations from the variety of steady solutions obtained in § 3.1. In the next section, we propose a methodology to obtain the full-scale design of the structure by fulfilling some objectives on the macroscopic behaviour of the steady flow, under the constraint of stable configuration.

4. From objectives to full-scale design

In the previous section, we performed a parametric study of the steady solution of (2.6) and (2.7) and the stability properties of the resulting wake, considering $\mathcal{L}$ and $\mathcal{F}$ as free parameters. In the present section, we outline a procedure for the objective-based full-scale design of a permeable circular membrane. We first define macroscopic objectives to be fulfilled and, performing microscopic simulations, we identify the geometry that best satisfies the macroscopic requirements. We consider cylindrical permeable shells formed by an array of elliptical inclusions, distributed with a constant angular distance, of axes l_t and l_n (normalized with the microscopic characteristic length) aligned along the tangential and normal directions to the membrane, respectively, in the range $0.02 < l_t,\ l_n < 0.98$.

4.1. *Choosing the design objective*

An important macroscopic property is the drag exerted on the solid structure by the incoming fluid. Several attempts of controlling this integral quantity, defined by (3.1), by permeable surfaces have been carried out, some of them focused on minimizing the drag (Garcia-Mayoral & Jiménez 2011; Abderrahaman-Elena & García-Mayoral 2017; Gómez-de Segura & García-Mayoral 2019), others investigating the conditions for drag maximization (Cummins *et al.* 2017, 2018).

We fix $Re = 100$ and we study the variation of C_D with $\mathcal{L}$ and $\mathcal{F}$. In figure 12 we report the iso-contours of C_D on the $(\mathcal{F}, \mathcal{L})$ plane. The bold solid line corresponds to the marginal stability boundary for $Re = 100$. Among all these possible solutions for the drag coefficient, we select the maximum value of the drag coefficient ($C_D = 1.339$), which occurs at $\mathcal{F} = 1.25 \times 10^{-2}$, $\mathcal{L} = 5 \times 10^{-3}$ (denoted by □ in figure 12) and in the following is compared with the full-scale simulations. For the sake of completeness, we select three other values of C_D denoted by ◯, ▷, ⋆ in figure 12, to verify the faithfulness of the homogenized model in the parameters space $(\mathcal{F}, \mathcal{L})$ for constant $\mathcal{L} = 10^{-4}$. Note that the case denoted with ⋆ is unstable, but we use it as an additional test case owing to the large recirculation region that this configuration exhibits.

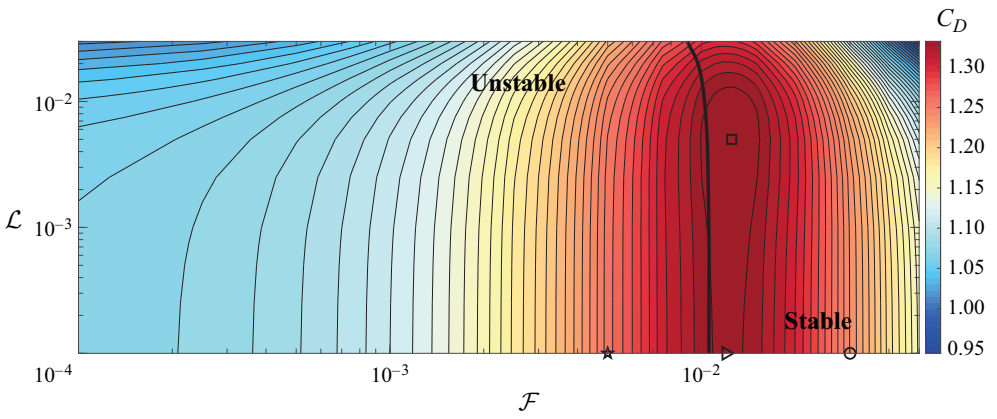

Figure 12. Iso-contours of C_D for $Re = 100$ in the $(\mathcal{F}, \mathcal{L})$ plane. Symbols identify the configurations listed in table 1. The marginal stability curve for the value of Re considered is represented by a bold solid line (all cases on the right-hand side of the curve are stable).

4.2. *Linking microscopic geometry to macroscopic properties: elliptical inclusions*

We now turn to describe the procedure for the determination of the microscopic geometry based on the macroscopic flow properties identified in the previous subsection. We first perform microscopic simulations in the domain depicted in figure 13(*a*) (dashed rectangle) whose lengths are non-dimensionalized with the microscopic length ℓ, so that the results do not depend on the separation-of-scales parameter $\varepsilon = \ell/D$, according to Zampogna & Gallaire (2020). Within this domain, two different microscopic problems need to be solved to calculate $\bar{F}_n$ and $\bar{L}_t$; they read respectively

$$\left.\begin{aligned} -\partial_i Q + \partial^2_{ll} F_i = 0, &\quad \text{in } \mathbb{F}, \\ \partial_i F_i = 0, &\quad \text{in } \mathbb{F}, \\ F_i = 0, &\quad \text{on } \partial\mathbb{M}, \\ \Sigma_{nn}(Q, \boldsymbol{F}) = -1, &\quad \text{on } \mathbb{U}, \\ \Sigma_{nn}(Q, \boldsymbol{F}) = 0, &\quad \text{on } \mathbb{D}, \\ F_i, Q, &\quad \text{periodic along } \boldsymbol{t}, \end{aligned}\right\} \tag{4.1}$$

and

$$\left.\begin{aligned} -\partial_i R + \partial^2_{ll} L_i = 0, &\quad \text{in } \mathbb{F}, \\ \partial_i L_i = 0, &\quad \text{in } \mathbb{F}, \\ L_i = 0, &\quad \text{on } \partial\mathbb{M}, \\ \Sigma_{tn}(R, \boldsymbol{L}) = -1, &\quad \text{on } \mathbb{U}, \\ \Sigma_{tn}(R, \boldsymbol{L}) = 0, &\quad \text{on } \mathbb{D}, \\ L_i, R, &\quad \text{periodic along } \boldsymbol{t}, \end{aligned}\right\} \tag{4.2}$$

where $i, l = t, n$, i.e. the equations are written in the local frame of reference of the cylinder surface. We refer to figure 13(*a*) for a definition of $\mathbb{F}, \mathbb{M}, \mathbb{U}$ and $\mathbb{D}$. In the microscopic problems (4.1) and (4.2) the scalar fields R and Q appear. They relate the value of the pressure on Γ_{int} to the upward and downward fluid stresses and do not contribute to the determination of the macroscopic flow through the membrane (see Zampogna & Gallaire

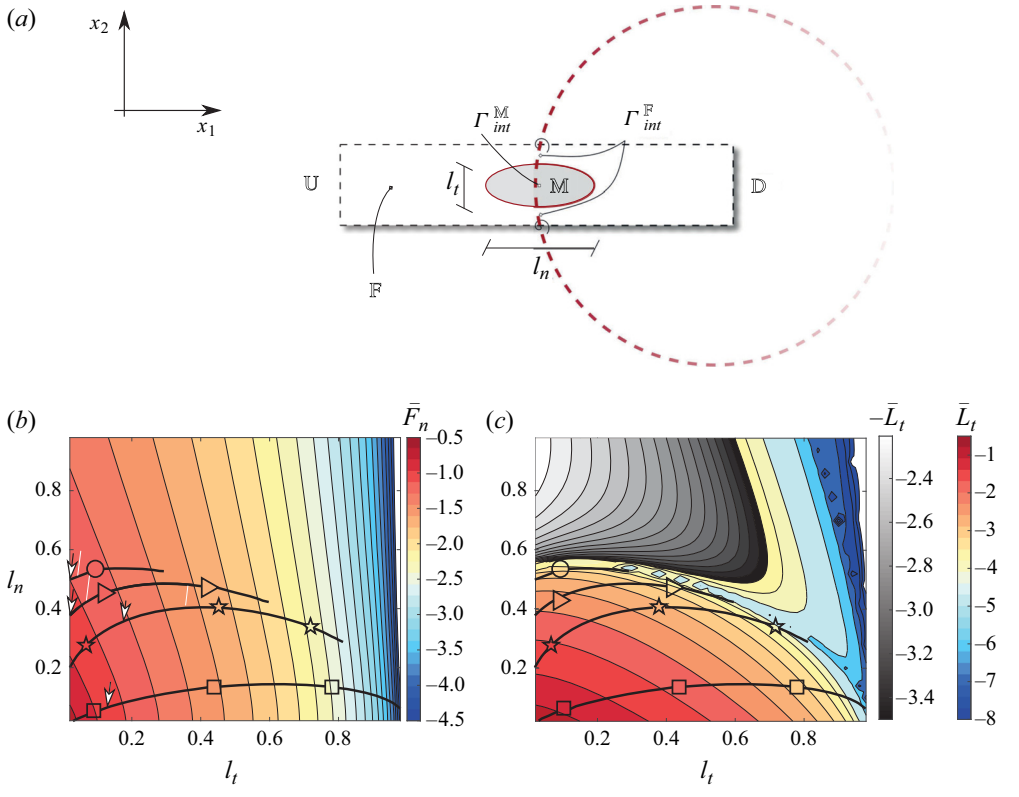

Figure 13. (*a*) Sketch of the membrane (red dashed line) with a zoom on the microscopic elementary cell used to calculate $\bar{L}_t$ and $\bar{F}_n$. The tangential- and normal-to-interface axes of the solid inclusion are respectively denoted with l_t and l_n and normalized by ℓ. Iso-contours of $\bar{F}_n = \mathcal{F}/\varepsilon$ (*b*) and $\bar{L}_t = \mathcal{L}/\varepsilon$ (*c*) on the plane (l_t, l_n), in logarithmic scale. Blue-to-red colours indicate positive values of $\bar{F}_n$ and $\bar{L}_t$ while grey-scale refers to negative values of $\bar{L}_t$. The lines identify the iso-contours of the possible couples (l_n, l_t) whose symbols correspond to different couples $(\mathcal{F}, \mathcal{L})$ of figure 12. Each point on those lines is a good candidate to realize the desired value of $\mathcal{F}$ and $\mathcal{L}$, upon adjustment of the value of ε. The selected values of l_t and l_n are labelled with white arrows for each case.

(2020) for a detailed explanation). For the purpose of the present work, we are not directly interested in microscopic fields representing the solution of these problems, but we need only to know the quantities $\bar{F}_n$ and $\bar{L}_t$ which appear in the macroscopic model via (2.9), where the symbol $\bar{\cdot}$ denotes the spatial average used in Zampogna & Gallaire (2020), i.e.

$$\bar{\cdot} = \lim_{\mathbb{U}\to\mathbb{D}} \frac{1}{|\mathbb{F}\cup\mathbb{M}|}\int_{\mathbb{F}} \cdot \,\mathrm{d}\boldsymbol{x} = \frac{1}{|\Gamma_{int}^{\mathbb{F}}\cup\Gamma_{int}^{\mathbb{M}}|}\int_{\Gamma_{int}^{\mathbb{F}}} \cdot \,\mathrm{d}\boldsymbol{x}, \tag{4.3}$$

with $\Gamma_{int}^{\mathbb{F}}$ and $\Gamma_{int}^{\mathbb{M}}$ the fluid and solid parts of Γ_{int} within the unit cell, as sketched in figure 13(*a*). The linear problems (4.1) and (4.2) are numerically solved for each couple (l_t, l_n), $0.02 < l_t,\ l_n < 0.98$ (with a step of 0.01), via their weak formulation implemented in the finite-element solver COMSOL Multiphysics. The spatial discretization is based on the Taylor–Hood (P2-P1) triangular elements for $\boldsymbol{F}$-$\boldsymbol{L}$ and R-Q, respectively. We refer to Zampogna & Gallaire (2020) for further details about the solution of the microscopic problems.

After averaging the solution of the microscopic problems, we deduce $\bar{F}_n$ and $\bar{L}_t$, whose iso-contours are reported in figure 13(*b*,*c*) as functions of the two axes l_n and l_t.

The parameters $\mathcal{F}$ and $\mathcal{L}$ are then calculated by a renormalization of $\bar{F}_n$ and $\bar{L}_t$ with respect to the macroscopic length scale, i.e.

$$\mathcal{F} = \varepsilon \bar{F}_n \quad \text{and} \quad \mathcal{L} = \varepsilon \bar{L}_t. \tag{4.4a,b}$$

While in a direct approach the parameters defining the full-scale geometry l_t, l_n and ε are given and the corresponding filtrability and slip numbers are evaluated, in the inverse procedure they need to be determined based on the choice of a given property that has to be satisfied by the fluid flow. Actually, there is no one-to-one relation linking $\mathcal{F}$ and $\mathcal{L}$ to the microscopic geometry. Once filtrability and slip are chosen, one has potentially full freedom in the choice of the microscopic structure. This choice is essentially related to the geometrical shape of the microscopic inclusions, in this case ellipsoidal ones with variable axes, and to their relative size with respect to the macroscopic length, as outlined in figure 13(*b*,*c*), where several configurations satisfy the desired values of $\mathcal{F}$ and $\mathcal{L}$, each one associated with a value of ε. For the sake of clarity we list the steps to follow in order to determine these geometrical parameters which allow us to define the microscopic geometry of the permeable shell:

(i) According to the previous subsection, we identify a pair $(\mathcal{F}, \mathcal{L}) = (\mathcal{F}^*, \mathcal{L}^*)$ of interest.

(ii) We find in the l_t–l_n plane the possible pairs of (l_t, l_n) that can give the correct set $(\mathcal{F}^*, \mathcal{L}^*)$. These values are found by evaluating the ratio $\mathcal{F}^*/\mathcal{L}^*$, which does not depend on ε (since F_n and L_t are proportional to ε). The potential values of l_n and l_t are those associated with the black solid lines in figure 13(*b*,*c*), which realize C_D^* upon renormalization by the proper value of ε that is still undetermined.

(iii) Among the potential candidates, the final value of ε and thus the values of (l_t, l_n) can be chosen based on other constraints (like, for instance, the minimization of microscopic anisotropy, i.e. $l_t \approx l_n$, the minimization of ε or the satisfaction of geometrical properties of the medium like the fluid-to-solid ratio).

(iv) Once the value of ε is selected, there is only one couple (l_t, l_n) that satisfies the macroscopic values of $\mathcal{F}^* = \varepsilon \bar{F}_n$ and $\mathcal{L}^* = \varepsilon \bar{L}_t$. We then deduce $\bar{F}_n$ and $\bar{L}_t$, and eventually l_t and l_n.

The values of ε, l_t and l_n are deduced for each case highlighted by the symbols in figure 12. Table 1 shows the values found for each case, corresponding to the white pointers in figure 13(*b*). For the cases denoted by ◯, ▷ and □ the values of (l_t, l_n) have been chosen so as to obtain a value of ε of order 10^{-1}, while for the case ⋆ the value of (l_t, l_n) guarantees minimal anisotropy with the constraint $\varepsilon \leq 0.045$.

The final full-scale geometries are thus obtained by distributing the inclusions along the membrane centreline Γ_{int}, with a constant angular distance among them given by $\Delta\phi = 2\pi\lfloor \varepsilon/\pi \rfloor$, with $\lfloor\cdot\rfloor$ the integer part in order to have an integer number of inclusions along the cylindrical shell. Two examples of microscopic geometries obtained are depicted in figure 14, where 69 and 32 inclusions are employed. Once the full-scale geometry is built, the reliability of the inverse procedure is verified as explained in the next section.

4.3. *Comparison between homogenized and full-scale results*

We verify the faithfulness of the homogenization approach and the subsequent retrieval of the microscopic geometry by comparing the results obtained using the equivalent model

	N	ε	l_t	l_n	$\mathcal{F}$	$\mathcal{L}$	C_D	C_D^{EQ}	L_R	L_R^{EQ}	X_R	X_R^{EQ}
⋆	69	4.49×10^{-2}	0.08	0.24	5.0×10^{-3}	1.0×10^{-4}	1.264	1.259	7.386	7.358	0.431	0.421
□	32	9.82×10^{-2}	0.12	0.06	1.25×10^{-2}	5.00×10^{-3}	1.338	1.339	—	—	—	—
▷	31	1.01×10^{-1}	0.02	0.38	1.2×10^{-2}	1.0×10^{-4}	1.350	1.334	—	—	—	—
◯	10	3.14×10^{-1}	0.02	0.50	3.0×10^{-2}	1.0×10^{-4}	1.365	1.239	—	—	—	—

Table 1. Relevant geometrical and physical parameters for the cases chosen in figure 12; N indicates the number of inclusions forming the membrane, the superscript ^{EQ} denotes quantities calculated using model (2.7) on Γ_{int} while the absence of superscript denotes quantities evaluated from the full-scale solution.

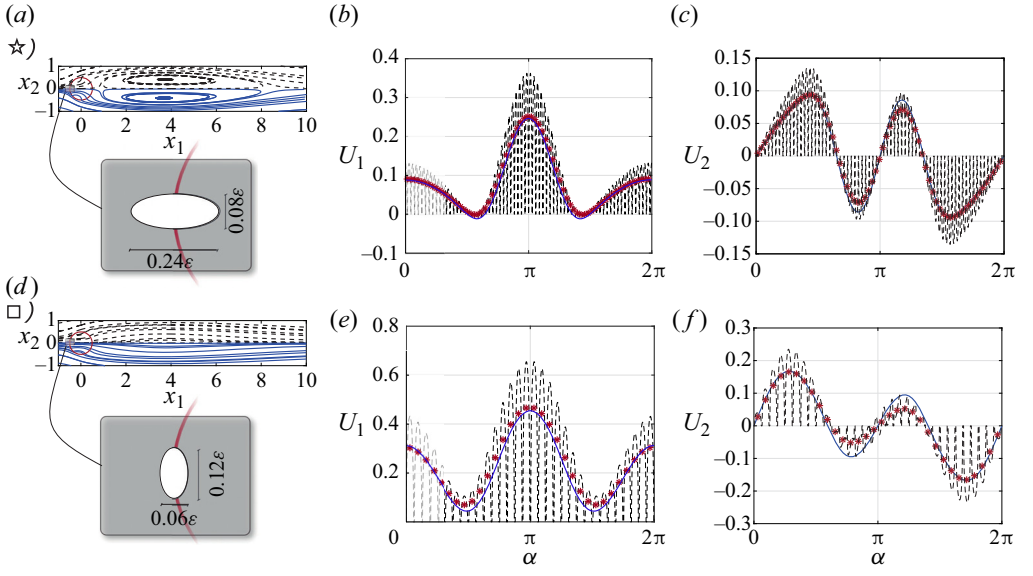

Figure 14. Comparison between full-scale and equivalent model for cases ⋆ and □ identified in figure 12. The microscopic geometry forming the cylindrical shell, sketched for each case in the grey insets on the left, is the result of the inverse procedure explained in § 4.2. (*a*,*d*) Flow streamlines for the full-scale case (black dashed lines) and for the macroscopic model (blue solid lines). (*b*,*c*,*e*,*f*) Horizontal and vertical velocities U_1 and U_2 sampled on the cylindrical shell using the angle α measured counterclockwise starting from the rear. Dashed lines represent the full-scale model, blue lines the macroscopic model and red stars the average of the full-scale model, calculated applying a discrete version of the integral in (4.3), based on a 1-point Gaussian rule, to the velocity profile in each microscopic elementary cell forming the membrane. Numerical values of ϵ, $\mathcal{F}$, $\mathcal{L}$ and other representative values of the fluid flow (C_D, X_R, L_R) are listed in table 1 for each case.

with the feature-resolved flow past the full-scale permeable shell. To deduce the full-scale flow, the Navier–Stokes equations are solved in the full-scale domain, where each solid inclusion forming the membrane is explicitly taken into account in the fluid domain and thus in the mesh. The full-scale problem is solved by the finite-element solver COMSOL Multiphysics, using the same numerical set-up as for the macroscopic flow solution. In order to have spatially converged results, mesh M1 (see Appendix A) has been modified in the vicinity of the full-scale structure. A circular refinement region of diameter $1.1L$ has been added with a resolution chosen in order to guarantee at least 10^2 cells between two adjacent solid inclusions whose boundary has been discretized using at least 50 segments. The boundary conditions on Γ_{in}, Γ_{out} and Γ_{lat} are the same as in the case of

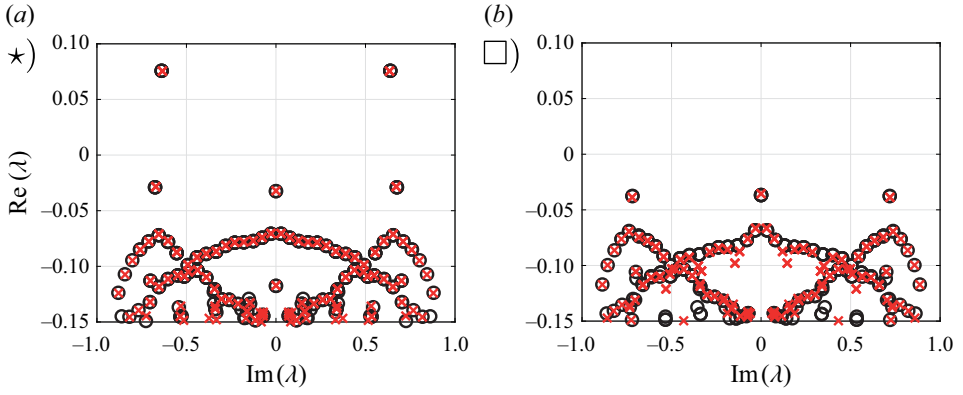

Figure 15. (*a*,*b*) Comparison between the homogenized and full-scale results of the stability analysis. The crosses and the circles denote the eigenvalues obtained from the full-scale structure and from the homogenized model, respectively, for the two reported cases.

the macroscopic model (2.7), while we impose a no-slip condition on the walls of each microscopic inclusion, i.e. $u_i|_{\Gamma_{\partial\mathbb{M}}} = 0$.

In figure 14 we report two sample comparisons of the flow fields obtained with the homogenized model and with the full-scale simulations (cases $\star$ and $\square$ identified in figure 12), together with the velocities at the membrane. In both cases, we observe a good agreement between the two approaches, with an error on the velocities along the membrane of the order of ε, as expected.

In table 1 we report the reference values (C_D, L_R, X_R) for all cases identified in figure 12. Also in this case, we observe an overall good agreement, even for extremely large values of ε, which are far beyond the rigorous domain of validity of the theory. Only for the case denoted by $\bigcirc$ are the differences in C_D non-negligible, suggesting that a maximum value of ε beyond which macroscopic model (2.7) is no more applicable lies between 10^{-1} and 3.5×10^{-1}. A complete validation also requires the comparison of the stability properties of the flow between homogenized model and full-scale simulations, reported in figure 15. We observe a good agreement between the spectra, and in particular the leading eigenvalues are well described by the homogenized model. Considering the one with largest real part, the relative errors on the absolute value are 0.25 % for the case $\star$ ($\lambda = 0.076 + 0.64\mathrm{i}$) and 0.6 % for the case $\square$ ($\lambda = -0.039 + 0.72\mathrm{i}$). We finally stress the importance of the validation described above, since it constitutes a strong proof of the faithfulness of the model developed in Zampogna & Gallaire (2020) in the case of flows with non-negligible macroscopic inertia.

In this section, we outlined a method for the geometrical reconstruction of the microscopic geometry based on the macroscopic properties of the membrane, thus concluding the first branch of the scheme described by figure 3. We note that the homogenized model, combined with the stability analysis technique, allows us to perform a parametric study spanning a very large range of possible geometries with extremely fast outputs. The flow through the resulting microscopic structure shows a good agreement with the homogenized model, thus giving confidence in the parametric study carried out in § 3. We verified the validity of the homogenized model through permeable membranes for Reynolds numbers of the order of 10^2. The error on the final solution is of order ε, thus degrading the solution when extremely large values of ε are considered. Nevertheless, the homogenized model gives also in these cases fairly reasonable results that can be

used as guidelines in a first parametric study, before optimizing the resulting microscopic structure.

The previous analysis was focused on membranes with monodisperse and identical microscopic inclusions along the centreline of the membrane. In the following, we analyse the opportunity to exploit membranes of variable permeability by employing a Lagrangian-based optimization, i.e. we focus on the second branch of the diagram of figure 3, in the inverse procedure part.

5. Adjoint-based optimization of membranes of variable properties

The purpose of the present section is to find profiles of $\mathcal{F}$ and $\mathcal{L}$ which are optimal with respect to a given objective, here specifically the maximization of the drag coefficient. To accomplish this task, a variational approach is used.

5.1. *Sensitivity with respect to variations of the slip and filtrability numbers*

In this section, we introduce the theoretical framework for the adjoint-based optimization of the structure of the membrane. We recall that, at the interface, we denote with superscript plus sign the variables evaluated in the inner part of the cylinder and with superscript minus sign those evaluated in the outer part. Any small modification $\delta\mathcal{M}_{ij}$ of the tensor component $\mathcal{M}_{ij}$ (i.e. variations of $\mathcal{F}$ or $\mathcal{L}$) induces a perturbation $(\delta\boldsymbol{u}, \delta p)$ on the flow field such that $(\boldsymbol{u}, p) = (\boldsymbol{U} + \delta\boldsymbol{u}, P + \delta p)$. The drag coefficient, i.e. the objective in the Lagrangian framework, is written as follows:

$$C_D = 2 \oint_{\Gamma_{cyl}} \left(\Sigma_{jk}\left(p^-, \boldsymbol{u}^-\right) - \Sigma_{jk}\left(p^+, \boldsymbol{u}^+\right)\right) n_k \delta_{1j} \,\mathrm{d}\Gamma. \tag{5.1}$$

The modification $\delta\mathcal{M}_{ij}$ thus perturbs the drag by δC_D according to

$$\delta C_D = 2 \oint_{\Gamma_{cyl}} \left(\Sigma_{jk}\left(\delta p^-, \delta\boldsymbol{u}^-\right) - \Sigma_{jk}\left(\delta p^+, \delta\boldsymbol{u}^+\right)\right) n_k \delta_{1j} \,\mathrm{d}\Gamma = \oint_{\Gamma_{cyl}} \nabla_{\mathcal{M}_{ij}} C_D \delta\mathcal{M}_{ij} \,\mathrm{d}\Gamma. \tag{5.2}$$

The quantities $(\delta\boldsymbol{u}^{\pm}, \delta p^{\pm})$ are the solution of (B3) reported in Appendix B, where a formal derivation of the sensitivity functions (i.e. the functions describing the variations of the objective C_D with respect to the control variable $\mathcal{F}$ and $\mathcal{L}$) is carried out. In the Lagrangian framework, the sensitivities of the drag coefficient with respect to variations of $\mathcal{L}$ and $\mathcal{F}$ are

$$\nabla_{\mathcal{F}} C_D = -Re u_i^{\dagger\dagger} \left(\Sigma_{jk}\left(P^-, \boldsymbol{U}^-\right) - \Sigma_{jk}\left(P^+, \boldsymbol{U}^+\right)\right) n_i n_j n_k \tag{5.3}$$

and

$$\nabla_{\mathcal{L}} C_D = Re u_i^{\dagger\dagger} \left(\Sigma_{jk}\left(P^-, \boldsymbol{U}^-\right) - \Sigma_{jk}\left(P^+, \boldsymbol{U}^+\right)\right) t_i t_j n_k, \tag{5.4}$$

where the Lagrange multipliers $(\boldsymbol{u}^{\dagger}, p^{\dagger}, \boldsymbol{u}^{\dagger\dagger})$, also called adjoint variables, are the solution of the following linear problem:

$$\left.\begin{gathered} \partial_i u_i^{\dagger} = 0, \quad u_j^{\dagger}\partial_i U_j - U_j \partial_j u_i^{\dagger} = \partial_i p^{\dagger} + \frac{1}{Re}\partial_{jj}^2 u_i^{\dagger} \quad \text{in } \Omega, \\ \left(\Sigma_{ik}\left(-p^{\dagger-}, \boldsymbol{u}^{\dagger-}\right) - \Sigma_{ik}\left(-p^{\dagger+}, \boldsymbol{u}^{\dagger+}\right)\right) n_k - u_i^{\dagger\dagger} = 0 \quad \text{on } \Gamma_{int}, \\ u_i^{\dagger+} = u_i^{\dagger-} \quad \text{on } \Gamma_{int} \end{gathered}\right\} \tag{5.5}$$

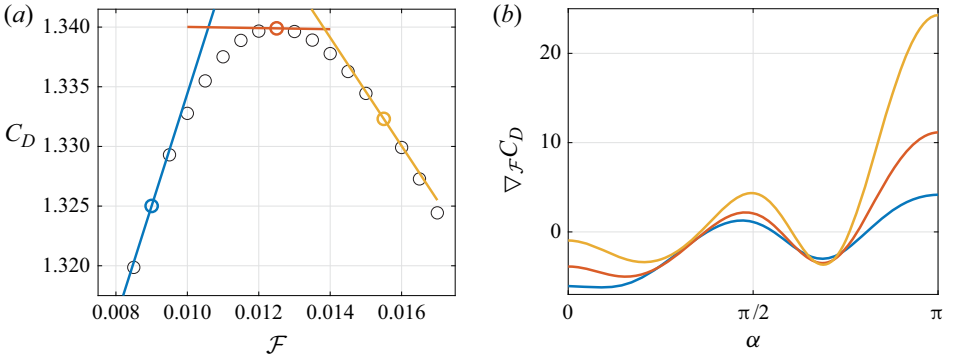

Figure 16. (*a*) Variation of the drag coefficient with $\mathcal{F}$, for $\mathcal{L} = 5 \times 10^{-3}$, directly evaluated from macroscopic model (2.6), (2.7) (black circles) and predictions of the gradient via the sensitivity approach (coloured lines) carried out around the configurations identified by coloured circles. (*b*) Distribution of sensitivity with respect to $\mathcal{F}$ along the $y > 0$ part of the cylinder, i.e. $0 < \alpha < \pi$, for the configurations denoted with colours in (*a*).

and

$$u_i^{\dagger\dagger} = Re^{-1} \mathcal{M}_{ji}^{-1} \left(u_j^{\dagger -} - 2\delta_{1j} \right) \quad \text{on } \Gamma_{int}, \tag{5.6}$$

together with the adjoint boundary conditions $u_i^{\dagger} = 0$ at the inflow, $\partial_2 u_1^{\dagger} = u_2^{\dagger} = 0$ at the transverse boundaries and $\Sigma_{ik}(-p^{\dagger}, \boldsymbol{u}^{\dagger}) n_k + u_k n_k u_i^{\dagger} = 0$ at the outflow. At this point, it is clear that in order to understand how the control variables $\mathcal{F}$ and $\mathcal{L}$ influence the objective function C_D via (5.3), (5.4), the linear problem (5.5) has to be solved, without the necessity of explicitly evaluating the perturbed state $(\boldsymbol{u}, p) = (\boldsymbol{U} + \delta\boldsymbol{u}, P + \delta p)$. The linear adjoint problem presents an advantage in terms of computational time with respect to the nonlinear problem for $(\boldsymbol{u}, p)$, and is suitable for a gradient-based optimization with a progressive update of the distribution of the membrane properties.

In figure 16(*a*) we report the variation of the drag coefficient with $\mathcal{F}$, for fixed $\mathcal{L} = 5 \times 10^{-3}$ (black dots), together with the prediction given by the sensitivity analysis (solid lines), close to the configuration of maximum C_D identified by the □ symbol in figure 12. Note that, at this stage, we keep $\mathcal{F}$ uniform along the membrane. A good agreement is observed, in the vicinity of the points where the sensitivity is evaluated, i.e. $\delta\mathcal{F} \approx 0.01\mathcal{F}$. The deviation becomes more important for variations larger than $\delta\mathcal{F} \approx 0.01\mathcal{F}$, showing a rather strong effect of nonlinearities close to the point of the maximum drag coefficient. In figure 16(*b*) we show the distribution of sensitivity along the upper part of the cylinder, for three cases. The distribution exhibits a non-monotonic behaviour, with positive values in the front and in the middle of the membrane, and negative values close to the rear of the cylinder.

The same analysis is performed for uniform variations of $\mathcal{L}$ (figure 17). In this case, we observe a monotonic behaviour, and the variations of the drag coefficient with $\mathcal{L}$ are considerably smaller than those observed when varying $\mathcal{F}$. The distribution, at low values of $\mathcal{L} \approx 5 \times 10^{-3}$, shows a peak at $\alpha \approx 130°$, which decreases with $\mathcal{L}$, and is negative in the other regions of the membrane.

In this section, we derived the sensitivity of the drag coefficient with respect to variations of $\mathcal{F}$ and $\mathcal{L}$. In the following, we exploit the sensitivity analysis to introduce a gradient-based optimization for the geometry of the membrane, when both the filtrability

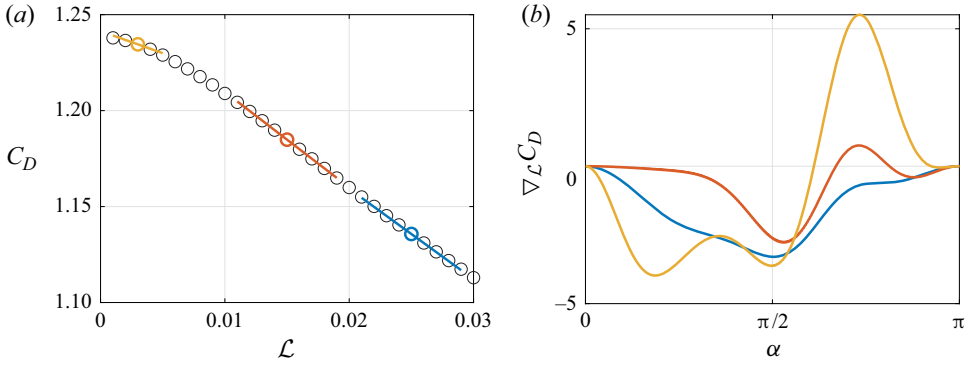

Figure 17. (*a*) Variation of the drag coefficient with $\mathcal{L}$, for $\mathcal{F} = 0.03$, directly evaluated from macroscopic model (2.6), (2.7) (black circles) and predictions of the gradient via the sensitivity approach (coloured lines) carried out around the corresponding coloured circles. (*b*) Distribution of sensitivity with respect to $\mathcal{L}$ along the $y > 0$ part of the cylinder, $0 < \alpha < \pi$.

and slip numbers are varied together, so as to find the optimal distribution of $\mathcal{F}$ and $\mathcal{L}$ to maximize the drag coefficient.

5.2. *Optimal distribution of the properties of the membrane*

The sensitivity functions found in the previous section are used here to obtain the optimal distributions of $\mathcal{F}$ and $\mathcal{L}$ that maximize the drag coefficient. The starting profiles of $\mathcal{F}$ and $\mathcal{L}$ for the gradient-based optimization are uniform. We chose different values of the initial guess, among which $\mathcal{F}^{(0)} = 1.25 \times 10^{-2}$ and $\mathcal{L}^{(0)} = 5 \times 10^{-3}$, i.e. the values that maximize C_D when the permeable membrane is formed by a repetition of a single microscopic inclusion (case denoted by the □ symbol in figure 12). We implement a gradient-ascent iterative procedure, using as initial guess $\mathcal{F}^{(0)}$ and $\mathcal{L}^{(0)}$. At each iteration (i), the values of the gradients $\nabla^{(i)}_{\mathcal{F}} C_D$ and $\nabla^{(i)}_{\mathcal{L}} C_D$ are evaluated by the adjoint analysis proposed above. We thus update the distribution of $\mathcal{F}$ and $\mathcal{L}$ in the direction of the gradient as follows:

$$\mathcal{F}^{(i+1)} = \mathcal{F}^{(i)} + \nabla^{(i)}_{\mathcal{F}} C_D \delta\mathcal{F} \quad \text{and} \quad \mathcal{L}^{(i+1)} = \mathcal{L}^{(i)} + \nabla^{(i)}_{\mathcal{L}} C_D \delta\mathcal{L}, \tag{5.7a,b}$$

with fixed step sizes $\delta\mathcal{F} = 10^{-2}\mathcal{F}^{(0)}$ and $\delta\mathcal{L} = 10^{-2}\mathcal{L}^{(0)}$. During the optimization procedure, the values of $\mathcal{F}$ and $\mathcal{L}$ have to remain strictly positive, to avoid non-physical values. Besides, too small or too large values jeopardize the inverse procedure, since large differences in the dimensions of the microscopic inclusions are difficult to handle without considering large values of the parameter ε, which degrade the accuracy of the homogenized model. Typical procedures to regularize the problem are based on the introduction of auxiliary variables to transform the inequality conditions into equality ones (Schulze & Sesterhenn 2013), or on the truncation of the gradient when the threshold values are reached (Lin 2007). In this work, for the sake of simplicity, we apply the latter procedure and we restrict the research of the optimal profiles to the intervals $10^{-3} < \mathcal{F}, \mathcal{L} < 1.5 \times 10^{-2}$. At each iteration, values of $\mathcal{F}$ or $\mathcal{L}$ larger (smaller) than the threshold value, due to an increase (decrease) along the gradient direction, are imposed to be equal to the threshold value. The iterative procedure is stopped when the relative difference between two successive evaluations of the drag coefficient is less than 10^{-4}.

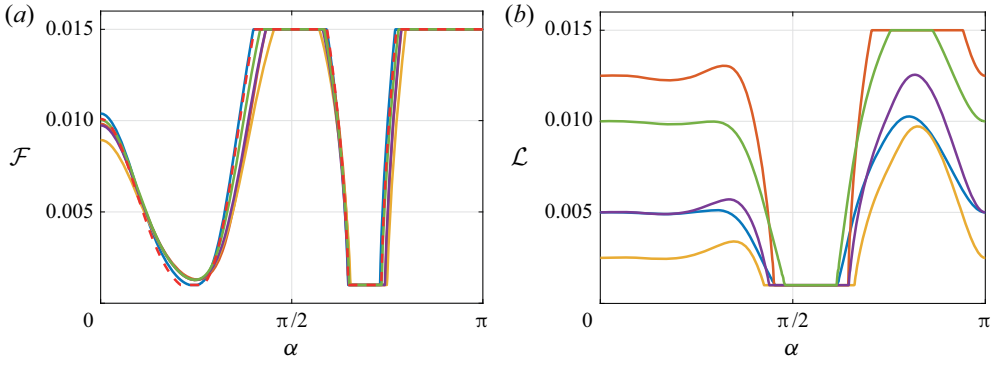

Figure 18. Results from the gradient-based optimization. Final distribution of (*a*) $\mathcal{F}$ and (*b*) $\mathcal{L}$, when both $\mathcal{F}$ and $\mathcal{L}$ are optimized for different initial guesses (coloured lines) and when only variations of $\mathcal{F}$ are considered with initial guess $\mathcal{F}^{(0)} = 0.0125$ and $\mathcal{L}^{(0)} = 0.005$ (red dashed line). The various initial guesses are $\mathcal{F}^{(0)} = 0.0125$ and $\mathcal{L}^{(0)} = 0.005$ (blue), $\mathcal{F}^{(0)} = 0.005$ and $\mathcal{L}^{(0)} = 0.0125$ (orange), $\mathcal{F}^{(0)} = 0.0025$ and $\mathcal{L}^{(0)} = 0.0025$ (yellow), $\mathcal{F}^{(0)} = 0.005$ and $\mathcal{L}^{(0)} = 0.005$ (purple), $\mathcal{F}^{(0)} = 0.01$, $\mathcal{L}^{(0)} = 0.01$ (green).

In figure 18 we report the optimal distribution of $\mathcal{F}$ and $\mathcal{L}$ along the semi-cylinder found via the iterative algorithm, for the optimization with both $\mathcal{F}$ and $\mathcal{L}$, with different initial guesses. Note that, depending on the initial value, a different number of iterations is needed to achieve convergence. While the final distribution of $\mathcal{F}$ does not show significant variations with the initial guess, the profiles of $\mathcal{L}$ are different. In the rear part, $0 < \alpha < \pi/2$, $\mathcal{L}$ remains constant and equal to the initial value. For $\alpha \approx \pi/2$, all distributions collapse to the lower threshold value, and in the front part they assume different values. However, the effect of the slip number on the final value of the drag coefficient (figure 19*a*) is small and the differences are below 0.5 %. Therefore, the effect of the filtrability is predominant and the optimal distribution of $\mathcal{F}$ is weakly influenced by $\mathcal{L}$. We thus consider the case in which the slip number is kept fixed, while the optimization is performed only on $\mathcal{F}$. The resulting distribution (red dashed line in figure 18*a*) is very similar to the other ones optimized with respect to both $\mathcal{F}$ and $\mathcal{L}$. Both approaches converge to a similar value of C_D (figure 19*b*), which is ≈ 6 % larger than the maximum drag obtained with uniform membrane properties. We therefore conclude that the optimization procedure leads to significantly larger values of C_D, in which the effect of the filtrability is predominant, with a weak dependence on the initial guess.

The increase of drag in the optimal configuration can be related to the previous observations in the case of constant filtrability. The optimization procedure tends to increase the filtrability in the front part ($\alpha \approx \pi$) of the cylinder and at $\alpha \approx \pi/2$, while it tends to decrease it at $\alpha \approx \pi/4$ and $\alpha \approx (3/4)\pi$. Compared with the constant filtrability case, the curvature of the streamlines is enhanced, thus leading to a more marked recompression in the inner part of the downstream portion of the membrane. This effect, leading to an increase of global drag, is enhanced in the optimal configuration since the flow is more constrained to pass through the front and the streamlines leave the cylinder through a narrower region, at $\alpha \approx \pi/2$, owing to the large values of filtrability in these regions. This constraint further magnifies the effects of the inner pressure gradients presented in the constant properties case. The analysis of the distributions of slip number shows that the drag is not influenced by variations of slip in the rear part of the cylinder.

In this section, we performed an adjoint-based optimization of the flow with respect to the drag. The typical computational time for one step of the optimization is equivalent to that of a steady calculation of the nonlinear Navier–Stokes equations, i.e. around

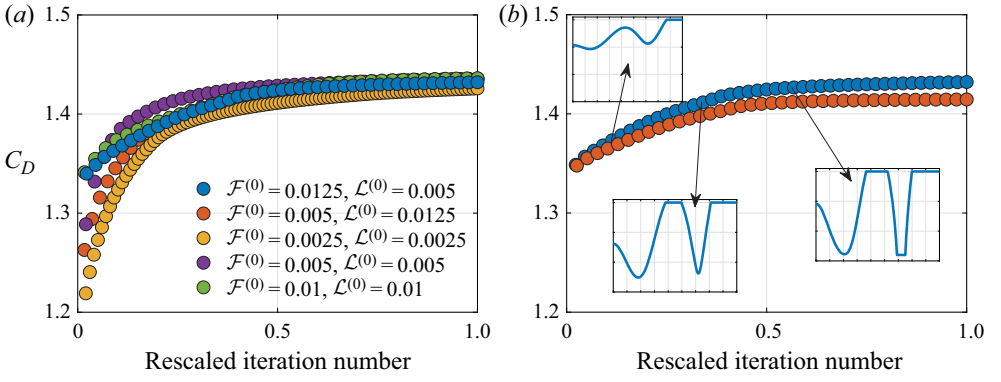

Figure 19. (*a*) Variation of the drag coefficient during the optimization procedure, for different initial guesses, as a function of the iteration number rescaled by the total number of iterations required to reach convergence. (*b*) Variation of the drag coefficient during the iterative procedure of the gradient-based optimization, when both $\mathcal{F}$ and $\mathcal{L}$ (blue dots) and only $\mathcal{F}$ (orange dots) are varied, with initial guess $\mathcal{F}^{(0)} = 0.0125$ and $\mathcal{L}^{(0)} = 0.005$. In the insets, we report the distributions of $\mathcal{F}$ for different iterations, the horizontal and vertical axes of the insets corresponding to $0 < \alpha < \pi$ and $0 < \mathcal{F} < 1.55 \times 10^{-2}$, respectively.

one minute for a common laptop computer. Since on average 30–60 iterations were needed to achieve convergence, with the presented simple algorithm, one optimization lasts for 30–60 minutes. The decoupling between microscopic properties and macroscopic effects on the flow allows one to move from a generic shape optimization problem to an optimization problem for the two scalar distributions $\mathcal{F}(\alpha)$ and $\mathcal{L}(\alpha)$, making the optimization procedure straightforward to implement compared with a full-scale case. Once the distribution of membrane properties is known, the inverse procedure has to be applied to choose the microscopic structure. In the following, we aim at retrieving an optimal full-scale structure of the membrane starting from the optimal profile of $\mathcal{F}$ found in the present section.

6. Full-scale design of membranes of variable properties

In order to fulfil the inverse procedure introduced in figure 3, we link the optimal distribution of filtrability and slip found in § 5.2 to a real full-scale structure of the permeable shell where the microscopic solid inclusions vary in shape and/or size. Since the effective stress jump condition developed by Zampogna & Gallaire (2020) has not been initially considered for membranes formed by solid inclusions of variable shape along the membrane, the first step to reach our objective is to modify and prove the validity of the macroscopic model for this case.

6.1. *Application of the effective stress jump model to the case of membranes with fast-varying microscopic geometry*

The easiest way to compute the microscopic tensors within the homogenization framework is to assume that the solid structure consists of a periodic repetition of a given unit cell (for a review, see Hornung (1997)). To relax this assumption one may assume that the variations of the microscopic structure are slow (e.g. Dalwadi, Bruna & Griffiths 2016) and hence solve the microscopic periodic problems (4.1) and (4.2) over each periodic unit cell and then compute the effective macroscopic tensors by averaging the microscopic solution over each cell. In the context of the present work, since fast variations of $\mathcal{F}$ and $\mathcal{L}$ can

be noticed in the optimal distributions of figure 18, we need a model to link the effective properties to the microscopic geometry, without any assumption about the nature of the variations of the inclusions along the membrane. The macroscopic model of Zampogna & Gallaire (2020) is adapted here so as to describe this case when the following hypotheses are valid:

(i) the permeable shell is the surface of a rotational body, whose radius is R;
(ii) the constraint $\ell/D \ll 1$ is still valid.

Under such assumptions, the macroscopic curvature is neglected in the microscopic domain as also done in Zampogna & Gallaire (2020) and the microscopic problems (4.1) and (4.2) are solved in the entire cylindrical shell, $\mathbb{F}_{tot}$, sketched in figure 20(b), defined as

$$\mathbb{F}_{tot} = \cup_{i=1}^{N} \mathbb{F}_i, \tag{6.1}$$

where $\mathbb{F}_i$ is the fluid domain within the ith unit cell sketched in figure 20(b) and N the total number of solid inclusions on the shell. On the left and right sides of $\mathbb{F}_{tot}$, we impose periodic boundary conditions as we are dealing with the surface of a rotational body. With these modifications, i.e. solving the microscopic problems (4.1) and (4.2) over $\mathbb{F}_{tot}$ instead of over each $\mathbb{F}_i$, the assumption of slow variations of the microscopic geometry is superfluous and a fast-varying microscopic geometry can be studied and associated with the optimal profile of $\mathcal{F}$ found in the previous subsection. To validate the model, we first calculate the microscopic quantities associated with two different distributions of solid inclusions along the membrane, D1 and D2. They represent an example of slow-varying (D1) and fast-varying (D2) microscopic geometries (see Appendix C). The distribution D1 is represented in the Cartesian frame of reference in figure 20(a) and in the local frame of reference of the cylinder in figure 20(b). The values of $\mathcal{F}$ and $\mathcal{L}$ for distributions D1 and D2 are shown in figures 21(a,b) and 21(c,d), respectively. While blue stars represent the values extracted from the solutions computed within $\mathbb{F}_{tot}$ by averaging over each unit cell, the light-blue circles represent the values of $\mathcal{F}$ and $\mathcal{L}$ deduced by classical calculations over each periodic unit cell $\mathbb{F}_i$. In the case of slow variations of the microscopic structure, the periodic problems (4.1) and (4.2) over the unit cell provide acceptable results for the effective tensors. Conversely, the important discrepancies between the blue and light-blue profiles represented in figure 21(c,d) show that fast variations of the microscopic geometries affect in a relevant way the values of the effective quantities $\mathcal{F}$ and $\mathcal{L}$ and microscopic problems (4.1) and (4.2) have to be computed over the entire microscopic domain $\mathbb{F}_{tot}$.

The last statement is supported by the comparison between the full-scale and the equivalent model that can be done once the effective values of $\mathcal{F}$ and $\mathcal{L}$ have been found. As shown in figure 22, the macroscopic velocities evaluated over the membrane are in perfect agreement with the full-scale profile for the case D1 of slow-varying geometries. The drag coefficient computed from the equivalent solution, C_D^{EQ}, is equal to 1.225, with a relative error with respect to the full-scale solution of $\approx 1.5\,\%$, in the order of the approximation. No substantial differences are noticed using the values of the effective tensor extracted from $\mathbb{F}_{tot}$ or from each periodic unit cell $\mathbb{F}_i$. In contrast, when distribution D2 is considered (figure 22c,d), the use of the effective tensor calculated within $\mathbb{F}_{tot}$ allows us to markedly reduce the error between the full-scale simulation and the macroscopic model.

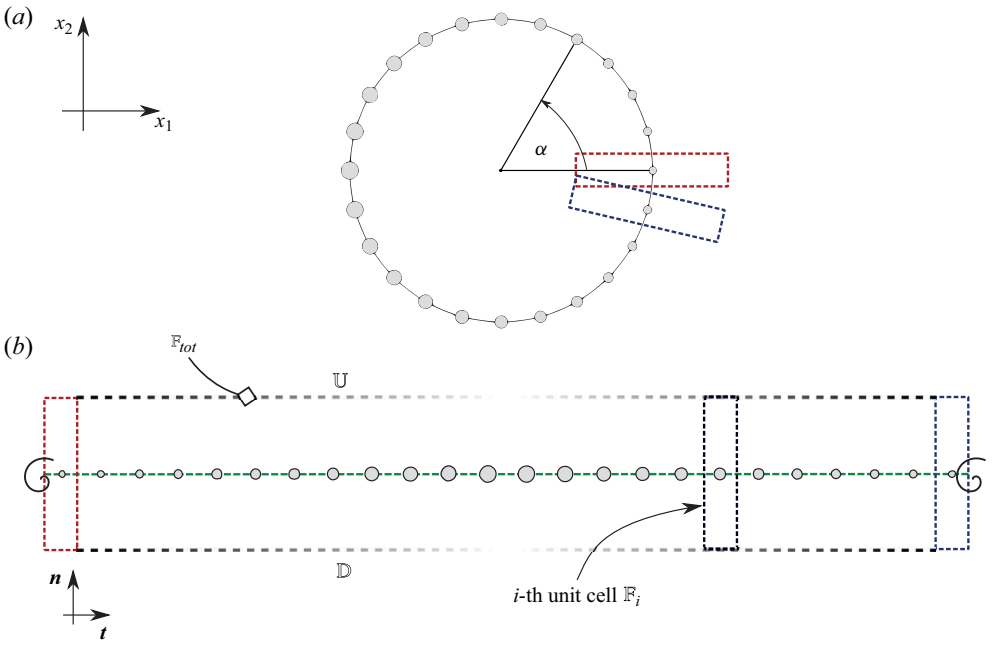

Figure 20. (*a*) Example of a cylindrical shell formed by variable microscopic inclusions, corresponding to distribution D1 in Appendix C. (*b*) Sketch of the microscopic domain, $\mathbb{F}_{tot}$, built by 'unrolling' the cylindrical shell (red and blue unit cells correspond to their 'rolled' counterpart in *a*). In order to deduce averaged profiles of F_n and L_t, the solution is averaged within each cell over the green dashed line.

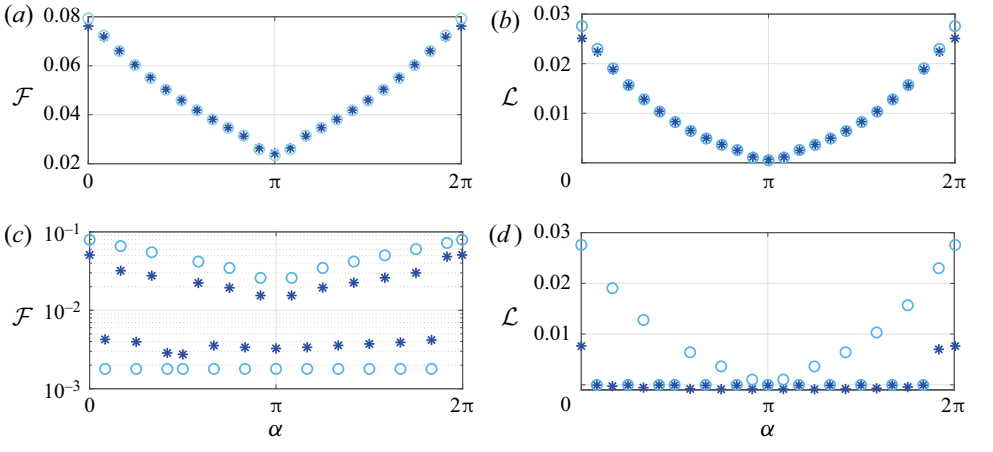

Figure 21. Values of $\mathcal{F}$ and $\mathcal{L}$ along $\mathbb{F}_{tot}$ (blue stars) and corresponding values computed within each cell $\mathbb{F}_i$ (light-blue circles) for distributions D1 (*a*,*b*) and D2 (*c*,*d*) described in Appendix C.

6.2. *Retrieving the full-scale microscopic geometry from the optimal $\mathcal{F}$–$\mathcal{L}$ profiles*

In the previous subsection we showed that the effective stress jump condition of Zampogna & Gallaire (2020) is reliable also in the case of fast-varying microscopic geometries when the adequate precautions described above are taken into account to formulate microscopic problems (4.1) and (4.2). We thus apply it to link the optimal distributions of effective filtrability and slip profiles found in § 5.2 to a distribution of microscopic solid

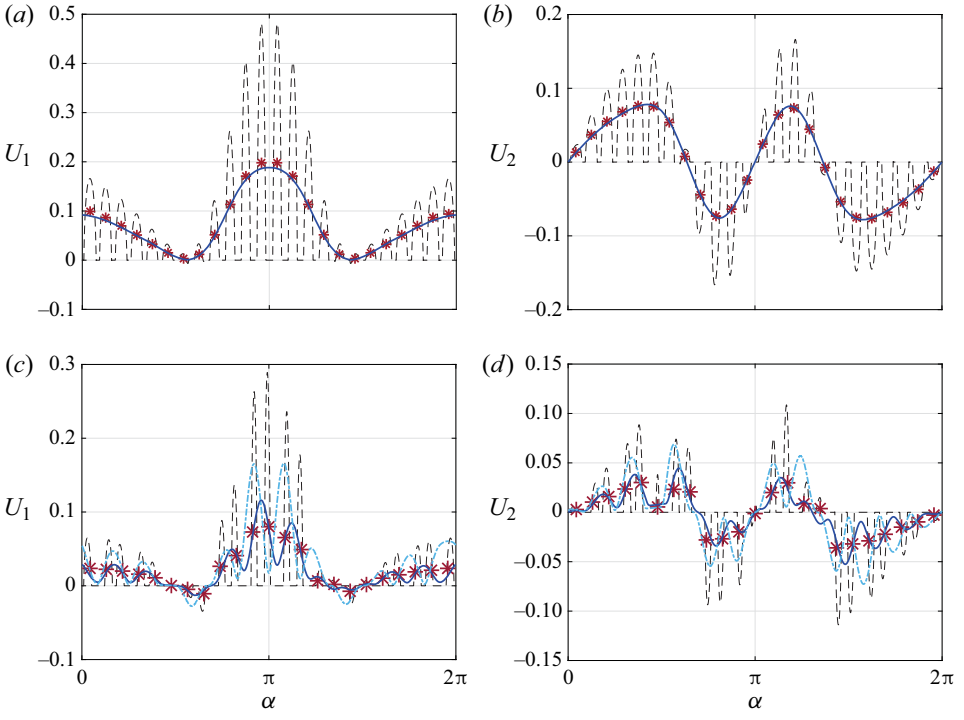

Figure 22. Comparison between the full-scale solution and the macroscopic model for distributions D1 (*a*,*b*) and D2 (*c*,*d*). All quantities are evaluated over the equivalent membrane Γ_{int}. Dashed lines represent the full-scale model, blue lines the macroscopic model where the values of the effective tensors have been calculated in $\mathbb{F}_{tot}$, light-blue dot-dashed lines correspond to the macroscopic model where the values of the effective tensors have been calculated in each periodic unit cell $\mathbb{F}_i$ and red stars represent the average of the full-scale model.

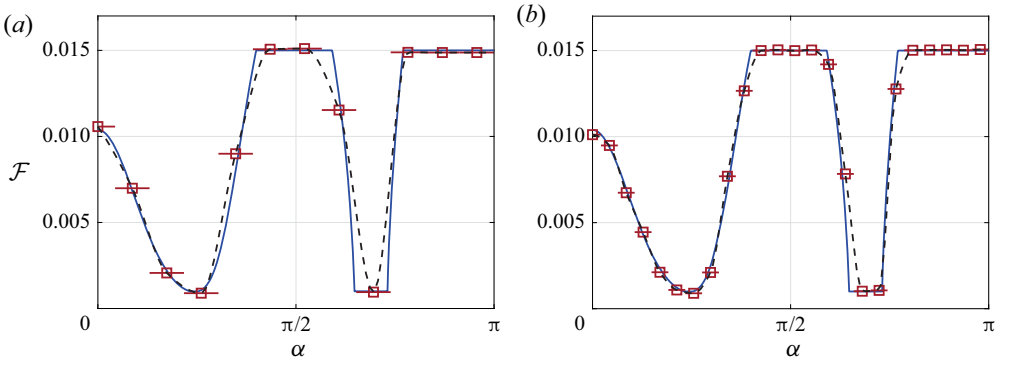

Figure 23. Variation of the optimal $\mathcal{F}$ profile with α. Blue lines correspond to the values of $\mathcal{F}$ found in § 5.2 while red squares to the values of $\mathcal{F}$ reconstructed from the microscopic problems in $\mathbb{F}_{tot}$. Black dashed lines correspond to the profiles reconstructed via a piecewise cubic interpolation of the red-square profile. (*a*) A total of 23 inclusions have been placed on the cylindrical shell ($\epsilon = 0.1369$); (*b*) 47 inclusions have been used ($\varepsilon = 0.0667$). A larger number of inclusions allows us to better reconstruct the $\mathcal{F}$ profile.

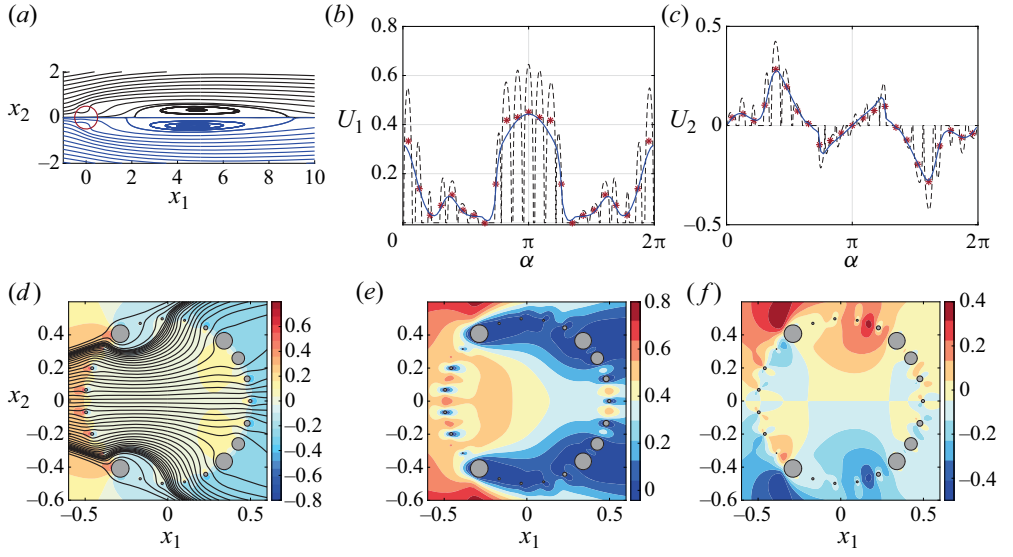

Figure 24. Flow past the optimal cylindrical structure deduced from the profile of $\mathcal{F}$ computed in § 5.2. A total of 23 solid inclusions (sketched in dark grey in *d–f*) have been placed on the cylinder leading to a value of ε equal to 0.137. (*a–c*) Comparison between full-scale and macroscopic solution. (*a*) The flow streamlines for the full-scale simulation (black lines) and for the macroscopic model (blue lines). (*b*,*c*) The horizontal and vertical velocities over Γ_{int}. Black dashed lines represent the full-scale solution, blue lines the macroscopic model, where $\mathcal{F}$ and $\mathcal{L}$ are evaluated using the reconstructed profiles (see figure 23), and red stars the averaged full-scale profile. Iso-contours of pressure (*d*), horizontal velocity (*e*) and vertical velocity (*f*) around the cylindrical shell. In (*d*) also flow streamlines within the shell have been represented to better appreciate the flow behaviour.

inclusions in order to design an optimal cylindrical membrane for drag maximization. For the sake of simplicity, we consider the case in which the optimization procedure is performed only on the value of $\mathcal{F}$, letting $\mathcal{L}$ vary according to the microscopic calculations. This allows us to focus our attention only on circular (rather than elliptical) inclusions of variable radius. As a consequence, the profile of $\mathcal{L}$ is unequivocally defined once the $\mathcal{F}$ profile is retrieved. This simplifying assumption has a marginal effect on the resulting optimal drag since the latter is only weakly affected by $\mathcal{L}$. Nevertheless, the following procedure can be straightforwardly generalized to variable distributions of both $\mathcal{F}$ and $\mathcal{L}$, by considering for instance elliptical inclusions as in § 4.2. The numerical implementation is based on a bisection method (see Appendix C), where at each iteration the value of the radius of each inclusion is adjusted so as to reach the aimed values of $\mathcal{F}$ up to a relative tolerance of 1 %. For the iterative procedure to be well defined, an initial guess has to be made. A good candidate is the value of $\mathcal{F}$ given by the case of perfectly periodic microstructures. The separation-of-scales parameter ε is a free parameter and has to be chosen to unequivocally define the radius of the solid inclusions. The resulting distributions are sketched in figure 23 for two different values of $\varepsilon = 0.1369$ and 0.0667, corresponding to 23 and 47 solid inclusions over the cylinder, respectively. We reconstruct the continuous $\mathcal{F}$ and $\mathcal{L}$ profiles via a piecewise-cubic interpolation (black dashed lines in figure 23) of the piecewise-constant values obtained from the solution of the microscopic problems averaged in each unit cell (red squares); however, we verified that the following results were not affected by a different choice of the interpolation. As a last check, we perform macroscopic and full-scale simulations in order to (i) confirm the validity of the model in this case and (ii) check that the full-scale geometry

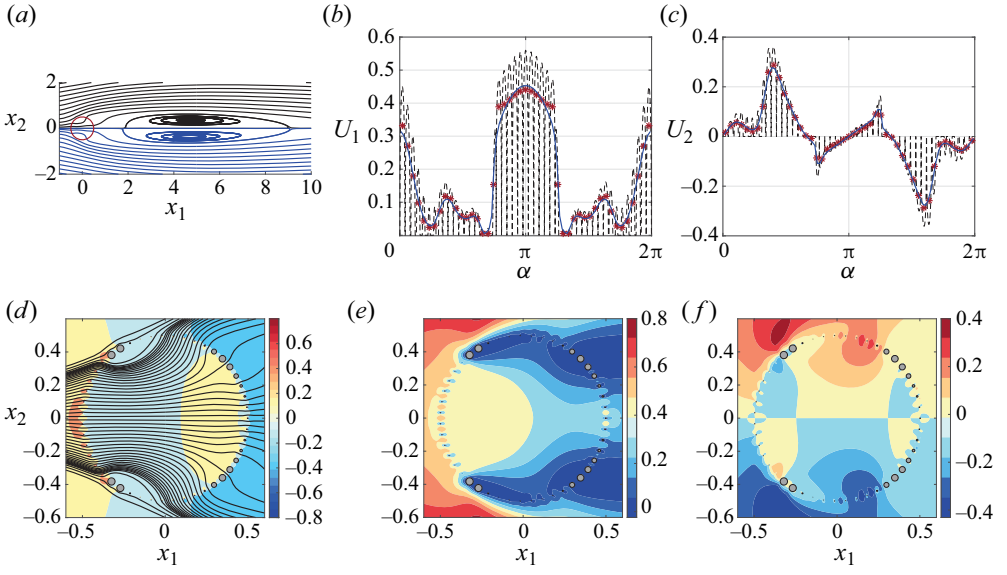

Figure 25. Same as figure 24 for a total number of 47 solid inclusions on the cylinder, leading to $\varepsilon = 0.066$.

actually maximizes the drag coefficient, as predicted in the Lagrangian-based optimization procedure. Figures 24 and 25 provide qualitative and quantitative information about the flow past the two retrieved full-scale optimal structures. According to figures 24(*a–c*) and 25(*a–c*), for both values of ε the full-scale solution reproduces well the behaviour and properties of the macroscopic flow calculated using the optimal profile of $\mathcal{F}$. The drag coefficients calculated over the two full-scale structures are $C_D^{\varepsilon=0.1369} = 1.427$ and $C_D^{\varepsilon=0.0667} = 1.412$, while the corresponding one estimated by the macroscopic model is equal to 1.414, exhibiting an error of about 1 % in the worst case. The variability of the microscopic inclusions is shown in figures 24(*d–f*) and 25(*d–f*), where a focus on the pressure and velocity fields across the cylindrical shell reveals the presence of local microscopic flow structures that become less and less important as ε decreases. We refer to Appendix C for the geometrical data used to build each full-scale structure and for their visualization.

These last findings accomplish the procedure sketched in figure 3. As previously shown, the inverse procedure admits multiple solutions, whose number can be further reduced by imposing other kinds of geometrical or functional constraints to the problem considered.

7. Conclusions and perspectives

In this work, we proposed an approach for the homogenization-based optimization of permeable membranes. We considered as a test case the wake flow past a permeable circular cylinder. The first part of the procedure was a parametric study of the steady-flow configurations and their stability with respect to perturbations. In this framework, the membrane was modelled by the effective stress jump interface condition developed in Zampogna & Gallaire (2020), for symmetric configurations with respect to the centreline of the membrane. Under these conditions, the membrane properties are described by two scalars, the filtrability and the slip numbers, the former representing the ability

of the fluid to pass through the membrane while the latter its ability to flow along the tangential-to-membrane direction. The flow morphology strongly resembles the one outlined in Ledda *et al.* (2018). The recirculation region past the cylinder detaches from the body and moves downstream, becomes smaller and disappears, as the filtrability number was increased. An increase in the slip number showed a decrease in the dimensions of the recirculation region. Interestingly, for large values of the filtrability number, the drag coefficient presents a maximum that is substantially larger than the drag coefficient of an impermeable cylinder. A bifurcation diagram was identified via the stability analysis, which unravelled the stabilization of the steady wake for large values of filtrability, a situation similar to the one outlined in Ledda *et al.* (2018). The unstable mode leads to a vortex shedding whose onset region moves downstream as the filtrability is increased.

Once the unstable configurations were excluded from the analysis, the second part of the work was focused on the reconstruction of the membrane based on the values of filtrability and slip numbers, identified to obtain proper macroscopic characteristics of the flow. We considered different test cases, among which the conditions that maximize the drag coefficient. We also outlined a procedure to recover the microscopic geometry that satisfies the constraints of filtrability and slip numbers, for elliptical inclusions. The agreement between the homogenized model and the full-scale simulations was very good, proving not only the faithfulness of the inverse procedure, but also the accuracy of the effective stress jump condition which was initially tested in Zampogna & Gallaire (2020) only in the Stokes flow regime.

The third part of the work was devoted to the optimization of a membrane whose filtrability and slip numbers were allowed to vary along the cylinder and to the reconstruction of the corresponding microscopic structure. As a test case, we considered as optimal objective the maximization of the drag coefficient. We first evaluated the sensitivity with respect to variations of the filtrability and slip numbers and thus performed a gradient-ascent optimization, using as initial guess the values of filtrability and slip numbers that maximize the drag in the case of constant membrane properties. In this test case, we obtained an increase in the drag coefficient of 6 % with respect to the case with constant membrane properties, and thus of 34 % with respect to the solid case. We then introduced a procedure to recover the microscopic structure that satisfies an optimal filtrability distribution, focusing on circular inclusions. The introduction of a new modified domain of validity of the microscopic problems associated with filtrability and slip numbers allowed us to correctly link these quantities to a full-scale geometry. Also in this case the agreement was fully satisfactory, thus validating the proposed approach for both constant and variable distributions of filtrability and slip numbers along the membrane.

This work aims at giving a rationale to the application of homogenized models to design membranes in the context of flow control, providing fast and accurate predictions and the opportunity to directly link macroscopic characteristics of the membrane to microscopic geometries. Because of the generality of the macroscopic model, real three-dimensional permeable shells can be handled at the cost of adding only one more parameter, representing the ability of the fluid to flow along the second tangent-to-membrane direction, much lower than the cost of adding approximately $1/\varepsilon$ degrees of freedom due to the meshing of a real full-scale three-dimensional membrane. The potential of the method stems from the decoupling between microscopic properties and macroscopic effects on the flow, which allows one to have a plethora of possible microscopic configurations giving the same macroscopic flow. This decoupling markedly simplifies the adjoint-based optimization procedure, allowing one to obtain

a single distribution of membrane properties which can be satisfied by an infinite number of possible microscopic geometries; the number of corresponding microscopic geometries can be further reduced by imposing other constraints. Despite the theoretical and analytical complexity of the homogenization technique, the final result consists of a simple boundary condition for the macroscopic flow model that enables the exploration of a vast range of geometrical configurations, with the great advantage of a marked reduction of the complexity and computational times needed to carry out the solution.

This work may be extended in several ways. The procedure explained here is a first step towards a rational design of membranes; if integrated with a model describing the equivalent transport of diluted substances across a permeable wall it represents a potential answer to the necessity identified in Park *et al.* (2017) to find the right balance of filtrability between a fluid and a diluted substance. The comparisons considered in the present paper show that the homogenized model well reproduces the flow behaviour in the case of inertial flows. The differences with respect to the full-scale solution are larger for cases in which the microscopic Reynolds number, $Re_{micro} = U\ell/\nu$, is large (for instance the case denoted by ◯ in table 1 where $Re_{micro} \approx 25$). This pushes us to proceed towards an extension of the model for high-Re flows, where the inertia of the flow within the membrane cannot be neglected (Zampogna & Bottaro 2016).

We conclude by observing that the interweaving of homogenization theory, bifurcation analysis and adjoint optimization methods showed great potential, opening up the path to a rational design of complex structures that can find a wide and varied range of applications in fluid dynamics.

Funding. This work was supported by the Swiss National Science Foundation (grant no. 200021_178971 to P.G.L. and grant no. 514636 to G.A.Z). F.G. and G.A.Z. acknowledge the EuroTech Postdoc Programme, co-funded by the European Commission under its framework programme Horizon 2020 (grant agreement no. 754462).

Declaration of interests. The authors report no conflict of interest.

Author ORCIDs.
Pier Giuseppe Ledda https://orcid.org/0000-0003-4435-8613;
E. Boujo https://orcid.org/0000-0002-4448-6140;
S. Camarri https://orcid.org/0000-0002-1946-5751;
F. Gallaire https://orcid.org/0000-0002-3029-1457;
G.A. Zampogna https://orcid.org/0000-0001-7570-9135.

Appendix A. Mesh convergence

In this appendix, we report the results of the mesh convergence. We considered the case $Re = 100$, $\mathcal{F} = 1.25 \times 10^{-2}$ and $\mathcal{L} = 5 \times 10^{-3}$. We verified both the convergence with respect to the size of the domain and with respect to the number of elements. The results are reported in table 2, for the drag coefficient and for the unstable eigenvalue studied in § 3.2. We initially increased the number of elements for the mesh M1, verifying the convergence. We therefore increased the domain size to verify its effect. We conclude that the number of elements and the size of the domain have a small impact on the base flow and global stability results, two significant digits remaining constant for every measured quantity. The mesh M1 (shown in figure 26) is suitable for the study and it has been used throughout the work.

Mesh	x_{1in}	x_{1out}	x_{2lat}	N_1	N_2	N_3	N_4	N_{int}	No. elements	C_D	Re(λ)	Im(λ)
M1	−30	90	25	1	1.25	5	13.3	31.9	144 008	1.339894	−0.03687	0.71985
M2	−30	90	25	1.25	1.55	6.3	16.7	39.8	161 896	1.339888	−0.03685	0.71980
M3	−30	90	25	1.5	1.9	7.5	20	47.8	187 498	1.339888	−0.03678	0.71986
M4	−30	90	25	2	2.5	10	26.7	63.7	241 094	1.339886	0.03673	0.71999
M1B	−45	120	37.5	1	1.25	5	13.3	31.9	164 918	1.333833	−0.03831	0.71867
M1C	−60	180	50	1	1.25	5	13.3	31.9	193 202	1.334047	−0.03843	0.71878

Table 2. Results of the mesh convergence. The edge densities are denoted with N, for different regions as depicted in figure 2.

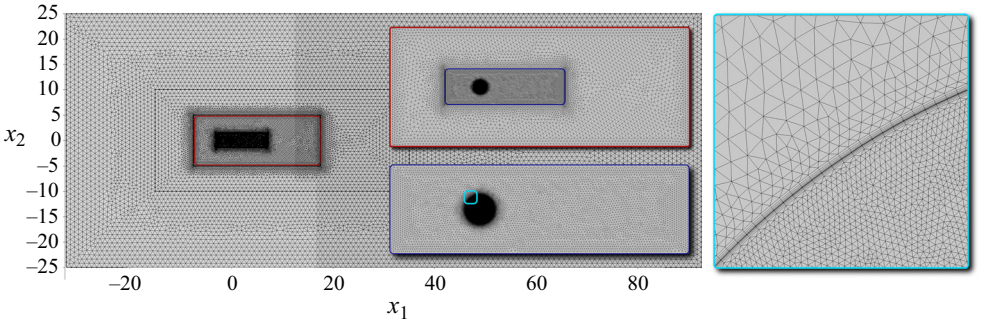

Figure 26. Overview of the mesh denoted by M1 in table 2 used for the macroscopic computations. In each coloured inset recursive magnifications approaching the cylinder are shown. In the light-blue inset prismatic layers adjacent to the fictitious interface Γ_{int} can be noticed; they have been added in order to well evaluate the normal-to-membrane fluid stress and integral quantities like the drag force acting on the cylinder.

Appendix B. Derivation of the sensitivity of the drag coefficient with respect to variations of the membrane properties

We propose here an extensive derivation of the sensitivity functions briefly introduced in § 5.2. For the sake of clarity, we recall that, at the interface, we denote with plus and minus sign superscripts the following limits:

$$f^- = \lim_{x_i \to \Gamma_{int}^-} f \quad \text{and} \quad f^+ = \lim_{x_i \to \Gamma_{int}^+} f, \tag{B1}$$

with Γ_{int}^- and Γ_{int}^+ the outer and inner sides of Γ_{int}. The drag coefficient, i.e. the objective in the Lagrangian framework, is defined in (5.1). According to this equation, any small modification of the tensor component $\mathcal{M}_{ij}$ modifies the drag by δC_D according to

$$\delta C_D = 2 \oint_{\Gamma_{cyl}} \left(\Sigma_{jk} \left(\delta p^-, \delta \boldsymbol{u}^- \right) - \Sigma_{jk} \left(\delta p^+, \delta \boldsymbol{u}^+ \right) \right) n_k \delta_{1j} \, \mathrm{d}\Gamma = \oint_{\Gamma_{cyl}} \nabla_{\mathcal{M}_{ij}} C_D \delta \mathcal{M}_{ij} \, \mathrm{d}\Gamma, \tag{B2}$$

where $(\delta \boldsymbol{u}^\pm, \delta p^\pm)$ is the linear perturbation to the base solution induced by the variation of the membrane tensor, whose governing equations can be deduced by substituting the

perturbed variables ($\boldsymbol{u} = \boldsymbol{U} + \delta\boldsymbol{u}, p = P + \delta p$) in (2.6), (2.7) and read

$$\left.\begin{aligned} \partial_i \delta u_i = 0, \quad \delta u_j \partial_j U_i + U_j \partial_j \delta u_i = -\partial_i \delta p + \frac{1}{Re}\partial^2_{jj}\delta u_i \quad &\text{in } \Omega, \\ \delta u_i^+ = \delta u_i^- = \delta u_i \quad &\text{on } \Gamma_{int}, \\ \delta u_i = Re\mathcal{M}_{ij}\left(\Sigma_{jk}\left(\delta p^-, \delta \boldsymbol{u}^-\right) - \Sigma_{jk}\left(\delta p^+, \delta \boldsymbol{u}^+\right)\right) n_k & \\ + Re\delta\mathcal{M}_{ij}\left(\Sigma_{jk}\left(p^-, \boldsymbol{u}^-\right) - \Sigma_{jk}\left(p^+, \boldsymbol{u}^+\right)\right) n_k \quad &\text{on } \Gamma_{int}, \end{aligned}\right\} \tag{B3}$$

together with boundary conditions $\delta u_i = 0$ at the inlet and $\Sigma_{jk}(\delta p, \delta \boldsymbol{u}) n_k = 0$ at the outflow.

We introduce the Lagrange multipliers $(\boldsymbol{u}^\dagger, p^\dagger, \boldsymbol{u}^{\dagger\dagger})$ referred to as the adjoint solution, and define the functional

$$\begin{aligned} \mathcal{J}\left(\boldsymbol{u}, p, \boldsymbol{u}^\dagger, p^\dagger, \boldsymbol{u}^{\dagger\dagger}, \mathcal{M}\right) = C_D & \\ - \int_\Omega p^\dagger \partial_i u_i \,\mathrm{d}\Omega & \\ - \int_\Omega u_i^\dagger \left(u_j \partial_j u_i - \partial_j \Sigma_{ij}\left(p, \boldsymbol{u}\right)\right) \mathrm{d}\Omega & \\ - \oint_{\Gamma_{int}} u_i^{\dagger\dagger} \left[u_i - Re\mathcal{M}_{ij}\left(\Sigma_{jk}\left(p^-, \boldsymbol{u}^-\right)\right.\right. & \\ \left.\left. - \Sigma_{jk}\left(p^+, \boldsymbol{u}^+\right)\right) n_k\right] \mathrm{d}\Gamma, & \end{aligned} \tag{B4}$$

whose gradient with respect to any variable f is

$$\frac{\partial \mathcal{J}}{\partial f}\delta f = \lim_{\epsilon \to 0} \frac{\mathcal{J}(f + \epsilon \delta f) - \mathcal{J}(f)}{\epsilon}. \tag{B5}$$

The variation of the drag coefficient thus reads

$$\delta C_D = \frac{\partial \mathcal{J}}{\partial\left(\boldsymbol{u}, p\right)}\delta\left(\boldsymbol{u}, p\right) + \frac{\partial \mathcal{J}}{\partial \mathcal{M}_{ij}}\delta\mathcal{M}_{ij}, \tag{B6}$$

since the gradient of the functional with respect to the adjoint variable is zero as long as the state equation is satisfied. The gradient with respect to $(\boldsymbol{u}, p)$ is

$$\begin{aligned} \frac{\partial \mathcal{J}}{\partial\left(\boldsymbol{u}, p\right)}\delta\left(\boldsymbol{u}, p\right) = 2 \oint_{\Gamma_{int}} \left(\Sigma_{ij}\left(\delta p^-, \delta \boldsymbol{u}^-\right) - \Sigma_{ij}\left(\delta p^+, \delta \boldsymbol{u}^+\right)\right) n_j \delta_{1i} \,\mathrm{d}\Gamma & \\ - \int_\Omega p^\dagger \partial_i \delta u_i \,\mathrm{d}\Omega & \\ - \int_\Omega u_i^\dagger \left(U_j \partial_j \delta u_i + \delta u_j \partial_j U_i - \partial_j \Sigma_{ij}\left(\delta p, \delta \boldsymbol{u}\right)\right) \mathrm{d}\Omega & \\ - \oint_{\Gamma_{int}} u_i^{\dagger\dagger} \left[\delta u_i^- - Re\mathcal{M}_{ij}\left(\Sigma_{jk}(\delta p^-, \delta \boldsymbol{u}^-) - \Sigma_{jk}(\delta p^+, \delta \boldsymbol{u}^+)\right) n_k\right] \mathrm{d}\Gamma. & \end{aligned} \tag{B7}$$

Integrating by parts and using the divergence theorem, we obtain analogous boundary terms at Γ_{int} for the inner and outer problems, to which we add those of the interface

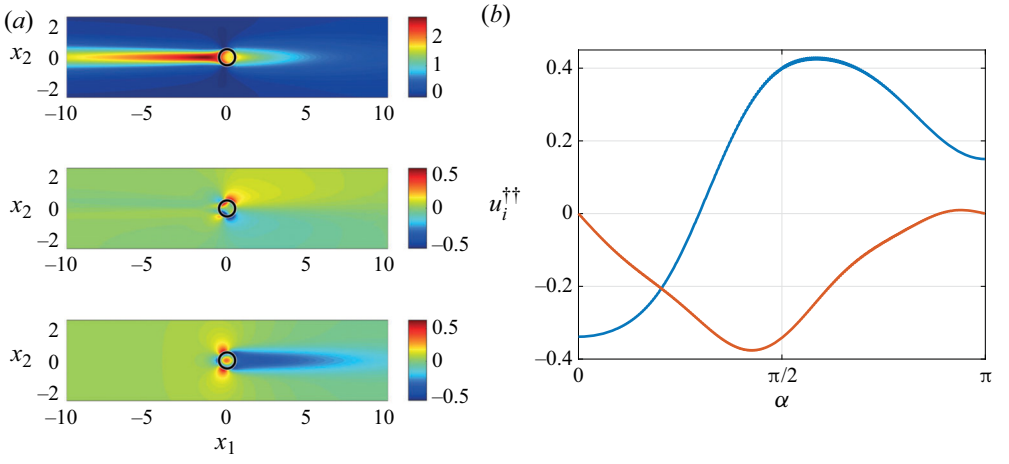

Figure 27. Adjoint field for $Re = 100$, $\mathcal{F} = 1.25 \times 10^{-2}$, $\mathcal{L} = 5 \times 10^{-3}$. (*a*) From top to bottom: $u_1^\dagger$, $u_2^\dagger$, $p^\dagger$; (*b*) $u_1^{\dagger\dagger}$ (blue curve) and $u_2^{\dagger\dagger}$ (orange curve) evaluated over Γ_{int} for $\alpha \in [0, \pi]$.

condition:

$$\begin{aligned}\frac{\partial \mathcal{J}}{\partial (\boldsymbol{u}, p)}\delta(\boldsymbol{u}, p) = &\oint_{\Gamma_{int}} \Sigma_{ij}\left(\delta p^-, \delta \boldsymbol{u}^-\right) n_j \left(2\delta_{i1} - u_i^{\dagger -} + u_k^{\dagger\dagger} Re \mathcal{M}_{ki}\right) \\ &+ \left(\Sigma_{ij}(-p^{\dagger -}, \boldsymbol{u}^{\dagger -}) n_j + U_k n_k u_i^{\dagger -} - u_i^{\dagger\dagger}\right) \delta u_i^- \, \mathrm{d}\Gamma \\ &- \oint_{\Gamma_{int}} \Sigma_{ij}\left(\delta p^+, \delta \boldsymbol{u}^+\right) n_j \left(2\delta_{i1} - u_i^{\dagger +} + u_k^{\dagger\dagger} Re \mathcal{M}_{ki}\right) \\ &+ \left(\Sigma_{ij}(-p^{\dagger +}, \boldsymbol{u}^{\dagger +}) n_j + (U_k n_k)\, u_i^{\dagger +}\right) \delta u_i^+ \, \mathrm{d}\Gamma \\ &+ \oint_{\partial\Omega} -\Sigma_{ij}\left(\delta p, \delta \boldsymbol{u}\right) n_j u_i^\dagger + \left(\Sigma_{ij}(-p^\dagger, \boldsymbol{u}^\dagger) n_j + U_k n_k u_i^\dagger\right) \delta u_i \, \mathrm{d}\Gamma \\ &+ \int_\Omega \partial_i u_i^\dagger \delta p \, \mathrm{d}\Omega \\ &- \int_\Omega u_j^\dagger \partial_i U_j - U_j \partial_j u_i^\dagger - \partial_i p^\dagger - \frac{1}{Re}\partial_{jj}^2 u_i^\dagger \delta u_i \, \mathrm{d}\Omega. \end{aligned} \tag{B8}$$

Exploiting the relation $\delta \boldsymbol{u} = \delta \boldsymbol{u}^+ = \delta \boldsymbol{u}^-$, cancelling the surface term on Ω and the boundary terms on Γ_{int} and $\partial\Omega$, we define $(\boldsymbol{u}^\dagger, p^\dagger)$ as the solution to the adjoint linear equations

$$\left.\begin{gathered} \partial_i u_i^\dagger = 0, \quad u_j^\dagger \partial_i U_j - U_j \partial_j u_i^\dagger = \partial_i p^\dagger + \frac{1}{Re}\partial_{jj}^2 u_i^\dagger \quad \text{in } \Omega, \\ \left(\Sigma_{ik}\left(-p^{\dagger -}, \boldsymbol{u}^{\dagger -}\right) - \Sigma_{ik}\left(-p^{\dagger +}, \boldsymbol{u}^{\dagger +}\right)\right) n_k - u_i^{\dagger\dagger} = 0 \quad \text{on } \Gamma_{int}, \\ u_i^{\dagger +} = u_i^{\dagger -} \quad \text{on } \Gamma_{int}, \end{gathered}\right\} \tag{B9}$$

with

$$u_i^{\dagger\dagger} = Re^{-1} \mathcal{M}_{ji}^{-1}\left(u_j^{\dagger -} - 2\delta_{1j}\right) \quad \text{on } \Gamma_{int}, \tag{B10}$$

i	D1	D2	D3	D4
1	0.10	0.10	0.070	0.0300
2	0.11	0.40	0.130	0.0320
3	0.12	0.12	0.280	0.0750
4	0.13	0.40	0.370	0.1170
5	0.14	0.14	0.090	0.2100
6	0.15	0.40	0.043	0.2750
7	0.16	0.40	0.050	0.3000
8	0.17	0.17	0.050	0.2300
9	0.19	0.40	0.390	0.0550
10	0.20	0.19	0.015	0.0150
11	0.22	0.40	0.063	0.0090
12	0.23	0.22	0.062	0.0135
13	0.22	0.40	0.062	0.0140
14	0.20	0.22	0.063	0.0110
15	0.19	0.40	0.015	0.0060
16	0.18	0.19	0.390	0.0500
17	0.17	0.40	0.050	0.3200
18	0.16	0.17	0.050	0.3300
19	0.15	0.40	0.043	0.0008
20	0.14	0.15	0.090	0.0085
21	0.13	0.40	0.370	0.0132
22	0.12	0.13	0.280	0.0149
23	0.11	0.40	0.130	0.0160
24	—	—	—	0.0160

Table 3. Values of the radius of the ith solid inclusion, non-dimensionalized with the microscopic length, for $i = 1, \ldots, 24$ for distributions D1, D2, D3 and D4. Note that, in distribution D4, 47 solid inclusions are present and the radius of the jth inclusion for $j = 25, \ldots, 47$ is equal to the radius of the ith inclusion, satisfying the formula $j = 47 - i + 1$.

together with adjoint boundary conditions $\boldsymbol{u}^\dagger = 0$ at the inflow and $\Sigma_{ik}(-p^\dagger, \boldsymbol{u}^\dagger)n_k + U_k n_k u_i^\dagger = 0$ at the outflow and lateral boundaries of the domain Γ_{lat}. We thus have

$$\delta C_D = \frac{\partial \mathcal{J}}{\partial \mathcal{M}_{ij}} \delta \mathcal{M}_{ij} = \oint_{\Gamma_{int}} u_i^{\dagger\dagger} Re \delta \mathcal{M}_{ij} \left(\Sigma_{jk}\left(P^-, \boldsymbol{U}^-\right) - \Sigma_{jk}\left(P^+, \boldsymbol{U}^+\right)\right) n_k \, \mathrm{d}\Gamma. \quad \text{(B11)}$$

Since $\mathcal{M}_{ij} = \mathcal{L} t_i t_j - \mathcal{F} n_i n_j$, we are able to evaluate the sensitivities with respect to $\mathcal{F}$ and $\mathcal{L}$ separately. Specializing (B11) for $\mathcal{F}$ we obtain

$$\delta C_D = \frac{\partial \mathcal{J}}{\partial \mathcal{F}} \delta \mathcal{F} = -\oint_{\Gamma_{int}} u_i^{\dagger\dagger} Re \delta \mathcal{F} n_i n_j \left(\Sigma_{jk}\left(P^-, \boldsymbol{U}^-\right) - \Sigma_{jk}\left(P^+, \boldsymbol{U}^+\right)\right) n_k \, \mathrm{d}\Gamma. \quad \text{(B12)}$$

The sensitivity with respect to $\mathcal{F}$ thus reads

$$\nabla_{\mathcal{F}} C_D = -Re u_i^{\dagger\dagger} n_i n_j \left(\Sigma_{jk}\left(P^-, \boldsymbol{U}^-\right) - \Sigma_{jk}\left(P^+, \boldsymbol{U}^+\right)\right) n_k, \quad \text{(B13)}$$

while, applying the same procedure with respect to $\mathcal{L}$, we obtain

$$\nabla_{\mathcal{L}} C_D = Re u_i^{\dagger\dagger} t_i t_j \left(\Sigma_{jk}\left(P^-, \boldsymbol{U}^-\right) - \Sigma_{jk}\left(P^+, \boldsymbol{U}^+\right)\right) n_k. \quad \text{(B14)}$$

It is finally clear that the gradients of C_D can be evaluated only if the solution of the adjoint problem (B9) is known. As a matter of example, in figure 27 we report the adjoint fields $(\boldsymbol{u}^\dagger, p^\dagger, \boldsymbol{u}^{\dagger\dagger})$ for $Re = 100$, $\mathcal{F} = 1.25 \times 10^{-2}$ and $\mathcal{L} = 5 \times 10^{-3}$.

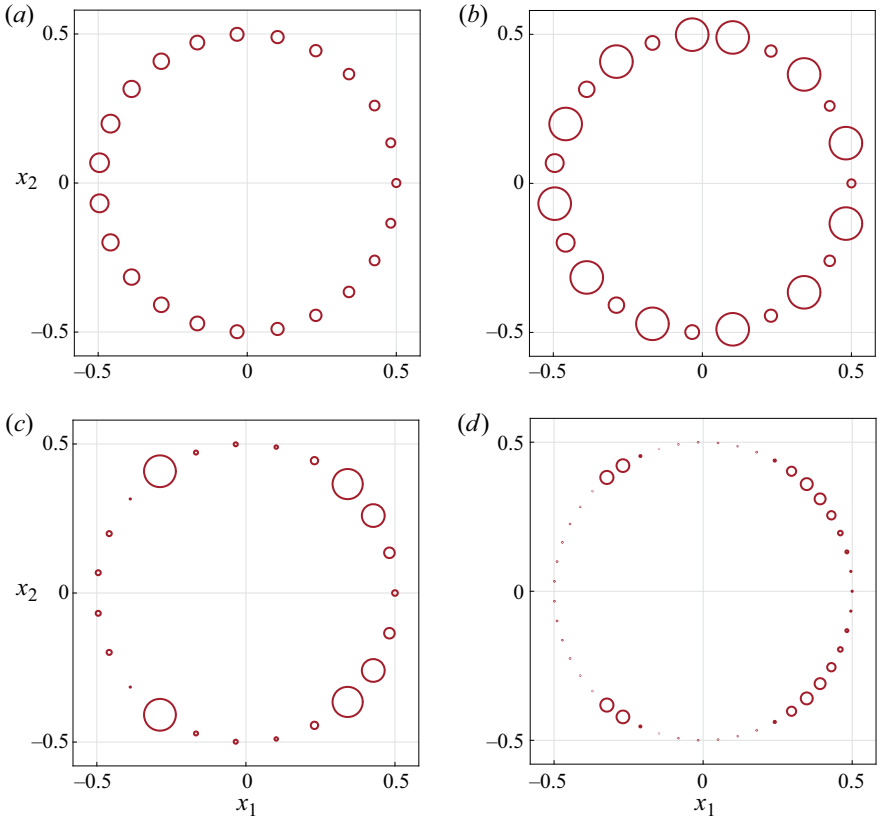

Figure 28. Visualization of the whole full-scale membrane geometry for configurations (*a*) D1, (*b*) D2, (*c*) D3 and (*d*) D4.

Appendix C. Geometrical data associated with the full-scale structures analysed in § 6

In § 6 different full-scale geometries with arbitrary varying solid inclusions have been proposed. Table 3 lists the parameters needed to build the cylindrical shell for each case. Distributions D1 and D2 correspond to test cases 1 and 2 that lead to the profiles of $\mathcal{F}$ and $\mathcal{L}$ depicted in figure 21, while distributions D3 and D4 correspond to the optimal full-scale structures found in § 6.2 with ϵ equal to 0.1369 and 0.0667, respectively. Each entry of the table contains the value of the radius of the ith circular solid inclusion, normalized by ℓ. The ith inclusion is positioned at an angle $\alpha = (2\pi/N)(i-1)$, where $N = 23$ for distributions D1, D2 and D3 and $N = 47$ for distribution D4. To have a visual idea of which kind of structures we are dealing with, in figure 28 a visualization of the corresponding full-scale membrane geometries is presented for the distributions listed in table 3.

For the sake of clarity we list the main steps of the bisection algorithm used to reconstruct the inclusions' distributions D3 and D4 listed in table 3. We denote with $R_i^{(m)}$ the radius of the ith inclusion forming the membrane, non-dimensionalized with the microscopic length, according to table 3. The superscript (m) is used here to denote the mth iteration of the bisection method.

(i) Two initial guess values are taken respectively equal to $R_i^{per} - \varepsilon R_i^{per}$ and $R_i^{per} + \varepsilon R_i^{per}$, where R^{per} is the radius of the inclusion which realizes the value $\mathcal{F}_i^{opt}$

as if the lattice was periodic, with $\mathcal{F}_i^{opt}$ the optimal filtrability evaluated in the ith cell.

(ii) At each iteration (m) and for every i the quantity $\mathcal{F}_i^{(m)}$ is evaluated by solving the microscopic problem (4.1) on the whole cylinder as explained in § 6.

(iii) If $\mathcal{F}_i^{(m)} - \mathcal{F}_i^{opt} < 0$ the radius of the ith inclusion at iteration (m) is decreased by a quantity $0.5|R_i^{(m)} - R_i^{(m-1)}|$.

(iv) If $\mathcal{F}_i^{(m)} - \mathcal{F}_i^{opt} > 0$ the radius of the ith inclusion at iteration (m) is increased by a quantity $0.5|R_i^{(m)} - R_i^{(m-1)}|$.

(v) The procedure is repeated until convergence, i.e. when $|\mathcal{F}_i^{(n)} - \mathcal{F}_i^{opt}|/|\mathcal{F}_i^{opt}| < \text{tol}$, where $\text{tol} = 0.01$.

References

Abderrahaman-Elena, N. & García-Mayoral, R. 2017 Analysis of anisotropically permeable surfaces for turbulent drag reduction. *Phys. Rev. Fluids* **2** (11), 114609.

Asadzadeh, S.S., Nielsen, L.T., Andersen, A., Dölger, J., Kiørboe, T., Larsen, P.S. & Walther, J.H. 2019 Hydrodynamic functionality of the lorica in choanoflagellates. *J. R. Soc. Interface* **16** (150), 20180478.

Baddoo, P.J, Hajian, R. & Jaworski, J.W 2021 Unsteady aerodynamics of porous aerofoils. *J. Fluid Mech.* **913**, A16.

Barkley, D. 2006 Linear analysis of the cylinder wake mean flow. *Europhys. Lett.* **75** (5), 750–756.

Barkley, D. & Henderson, R.D. 1996 Three-dimensional floquet stability analysis of the wake of a circular cylinder. *J. Fluid Mech.* **322**, 215–241.

Barta, E. & Weihs, D. 2006 Creeping flow around a finite row of slender bodies in close proximity. *J. Fluid Mech.* **551**, 1–17.

Bongarzone, A., Bertsch, A., Renaud, P. & Gallaire, F. 2021 Impinging planar jets: hysteretic behaviour and origin of the self-sustained oscillations. *J. Fluid Mech.* **913**, A51.

Boujo, E., Ehrenstein, U. & Gallaire, F. 2013 Open-loop control of noise amplification in a separated boundary layer flow. *Phys. Fluids* **25** (12), 124106.

Boujo, E. & Gallaire, F. 2014 Controlled reattachment in separated flows: a variational approach to recirculation length reduction. *J. Fluid Mech.* **742**, 618–635.

Boujo, E. & Gallaire, F. 2015 Sensitivity and open-loop control of stochastic response in a noise amplifier flow: the backward-facing step. *J. Fluid Mech.* **762**, 361–392.

Brinkman, H.C. 1949 A calculation of the viscous force exerted by a flowing fluid on a dense swarm of particles. *Flow Turbul. Combust.* **1** (1), 27.

Camarri, S. & Iollo, A. 2010 Feedback control of the vortex-shedding instability based on sensitivity analysis. *Phys. Fluids* **22** (9), 094102.

Castro, I.P. 1971 Wake characteristics of two-dimensional perforated plates normal to an air-stream. *J. Fluid Mech.* **46** (3), 599–609.

Chomaz, J-M 2005 Global instabilities in spatially developing flows: non-normality and nonlinearity. *Annu. Rev. Fluid Mech.* **37** (1), 357–392.

Crabill, J., Witherden, F.D. & Jameson, A. 2018 A parallel direct cut algorithm for high-order overset methods with application to a spinning golf ball. *J. Comput. Phys.* **374**, 692–723.

Cummins, C., Seale, M., Macente, A., Certini, D., Mastropaolo, E., Viola, I.M. & Nakayama, N. 2018 A separated vortex ring underlies the flight of the dandelion. *Nature* **562** (7727), 414–418.

Cummins, C., Viola, I.M., Mastropaolo, E. & Nakayama, N. 2017 The effect of permeability on the flow past permeable disks at low Reynolds numbers. *Phys. Fluids* **29**, 097103.

Dalwadi, M.P., Bruna, M. & Griffiths, I.M. 2016 A multiscale method to calculate filter blockage. *J. Fluid Mech.* **809**, 264–289.

Darcy, H. 1856 *Les fontaines publiques de la ville de Dijon: exposition et application des principes a suivre et des formules a employer dans les questions de distribution d'eau*. Victor Dalmont.

Elimelech, M. & Phillip, W. 2011 The future of seawater desalination: energy, technology, and the environment. *Science* **333**, 712–717.

Ellington, C.P. 1980 Wing mechanics and take-off preparation of thrips (thysanoptera). *J. Expl Biol.* **85** (1), 129–136.

FORNBERG, B. 1980 A numerical study of steady viscous flow past a circular cylinder. *J. Fluid Mech.* **98** (4), 819–855.

FRITZMANN, C., LÖWENBERG, J., WINTGENS, T. & MELIN, T. 2007 State-of-the-art of reverse osmosis desalination. *Desalin.* **216**, 1–76.

GARCIA-MAYORAL, R. & JIMÉNEZ, J. 2011 Drag reduction by riblets. *Phil. Trans. R. Soc.* A **369** (1940), 1412–1427.

GIANNETTI, F. & LUCHINI, P. 2007 Structural sensitivity of the first instability of the cylinder wake. *J. Fluid Mech.* **581**, 167–197.

HAJIAN, R. & JAWORSKI, J.W 2017 The steady aerodynamics of aerofoils with porosity gradients. *Proc. R. Soc.* A **473** (2205), 20170266.

HORNUNG, U. 1997 *Homogenization and Porous Media*. Springer.

ICARDI, M., BOCCARDO, G., MARCHISIO, D.L., TOSCO, T. & SETHI, R. 2014 Pore-scale simulation of fluid flow and solute dispersion in three-dimensional porous media. *Phys. Rev.* E **90**, 013032.

IUNGO, G.V., VIOLA, F., CAMARRI, S., PORTÉ-AGEL, F. & GALLAIRE, F. 2013 Linear stability analysis of wind turbine wakes performed on wind tunnel measurements. *J. Fluid Mech.* **737**, 499–526.

JACKSON, C.P. 1987 A finite-element study of the onset of vortex shedding in flow past variously shaped bodies. *J. Fluid Mech.* **182**, 23–45.

JAWORSKI, J.W. & PEAKE, N. 2020 Aeroacoustics of silent owl flight. *Annu. Rev. Fluid Mech.* **52** (1), 395–420.

JENSEN, K.H., BERG-SØRENSEN, K., BRUUS, H., HOLBROOK, N.M., LIESCHE, J., SCHULZ, A., ZWIENIECKI, M.A. & BOHR, T. 2016 Sap flow and sugar transport in plants. *Rev. Mod. Phys.* **88**, 035007.

JONES, S.K., YUN, Y.J.J., HEDRICK, T.L., GRIFFITH, B.E. & MILLER, L.A. 2016 Bristles reduce the force required to 'fling' wings apart in the smallest insects. *J. Expl Biol.* **219** (23), 3759–3772.

LABBÉ, R & DUPRAT, C 2019 Capturing aerosol droplets with fibers. *Soft Matt.* **15** (35), 6946–6951.

LĀCIS, U. & BAGHERI, S. 2017 A framework for computing effective boundary conditions at the interface between free fluid and a porous medium. *J. Fluid Mech.* **812**, 866–889.

LĀCIS, U., ZAMPOGNA, G.A. & BAGHERI, S. 2017 A computational continuum model of poroelastic beds. *Proc. R. Soc.* A **473** (2199), 20160932.

LĀCIS, U., SUDHAKAR, Y., PASCHE, S. & BAGHERI, S. 2020 Transfer of mass and momentum at rough and porous surfaces. *J. Fluid Mech.* **884**, A21.

LEDDA, P.G., SICONOLFI, L., VIOLA, F., CAMARRI, S. & GALLAIRE, F. 2019 Flow dynamics of a dandelion pappus: A linear stability approach. *Phys. Rev. Fluids* **4**, 071901.

LEDDA, P.G., SICONOLFI, L., VIOLA, F., GALLAIRE, F. & CAMARRI, S. 2018 Suppression of von kármán vortex streets past porous rectangular cylinders. *Phys. Rev. Fluids* **3**, 103901.

LEMKE, M., REISS, J. & SESTERHENN, J. 2014 Adjoint based optimisation of reactive compressible flows. *Combust. Flame* **161** (10), 2552–2564.

LIN, C.-J. 2007 Projected gradient methods for nonnegative matrix factorization. *Neural Comput.* **19** (10), 2756–2779.

LUCHINI, P. & BOTTARO, A. 2014 Adjoint equations in stability analysis. *Annu. Rev. Fluid Mech.* **46** (1), 493–517.

MARQUET, O., SIPP, D. & JACQUIN, L. 2008 Sensitivity analysis and passive control of cylinder flow. *J. Fluid Mech.* **615**, 221–252.

MATIN, A., KHAN, Z., ZAIDIA, S.M.J. & BOYCE, M.C. 2011 Biofouling in reverse osmosis membranes for seawater desalination: phenomena and prevention. *Desalin.* **281**, 1–16.

MELIGA, P., BOUJO, E., PUJALS, G. & GALLAIRE, F. 2014 Sensitivity of aerodynamic forces in laminar and turbulent flow past a square cylinder. *Phys. Fluids* **26** (10), 104101.

MELIGA, P., CHOMAZ, J.-M. & SIPP, D. 2009 Unsteadiness in the wake of disks and spheres: instability, receptivity and control using direct and adjoint global stability analyses. *J. Fluids Struct.* **25** (4), 601–616.

MELIGA, P., SIPP, D. & CHOMAZ, J.-M. 2010 Open-loop control of compressible afterbody flows using adjoint methods. *Phys. Fluids* **22** (5), 054109.

MONKEWITZ, P.A. 1988 The absolute and convective nature of instability in two dimensional wakes at low Reynolds numbers. *Phys. Fluids* **31** (5), 999–1006.

NEMILI, A., ÖZKAYA, E., GAUGER, N., THIELE, F. & CARNARIUS, A. 2011 Optimal control of unsteady flows using discrete adjoints. In *41st AIAA Fluid Dynamics Conference And Exhibit, AIAA paper* 2011-3720.

NICOLLE, A. & EAMES, I. 2011 Numerical study of flow through and around a circular array of cylinders. *J. Fluid Mech.* **679**, 1–31.

NORBERG, C. 2003 Fluctuating lift on a circular cylinder: review and new measurements. *J. Fluids Struct.* **17** (1), 57–96.

OLIVIER, J. 2004 Fog harvesting: an alternative source of water supply on the west coast of South Africa. *GeoJ.* **61** (2), 203–214.

PARK, H.B., KAMCEV, J., ROBESON, L.M., ELIMELECH, M. & FREEMAN, B.D. 2017 Maximizing the right stuff: the trade-off between membrane permeability and selectivity. *Science* **356**, eaab0530.

PARK, K-C, CHHATRE, S.S., SRINIVASAN, S., COHEN, R.E. & MCKINLEY, G.H. 2013 Optimal design of permeable fiber network structures for fog harvesting. *Langmuir* **29** (43), 13269–13277.

PASCHE, S., AVELLAN, F. & GALLAIRE, F. 2017 Part load vortex rope as a global unstable mode. *Trans. ASME: J. Fluids Engng* **139** (5), 051102.

PEZZULLA, M., STRONG, E.F., GALLAIRE, F. & REIS, P.M. 2020 Deformation of porous flexible strip in low and moderate Reynolds number flows. *Phys. Rev. Fluids* **5**, 084103.

PROVANSAL, M., MATHIS, C. & BOYER, L. 1987 Bénard-von kármán instability: transient and forced regimes. *J. Fluid Mech.* **182**, 1–22.

QUARTERONI, A. 2017 *Domain Decomposition Methods*, pp. 555–612. Springer International Publishing.

RAHARDIANTO, A., MCCOOL, B.C. & COHEN, Y. 2010 Accelerated desupersaturation of reverse osmosis concentrate by chemically-enhanced seeded precipitation. *Desalin.* **264**, 256–267.

SCHULZE, J. & SESTERHENN, J. 2013 Optimal distribution of porous media to reduce trailing edge noise. *Comput. Fluids* **78**, 41–53, lES of turbulence aeroacoustics and combustion.

GÓMEZ-DE SEGURA, G. & GARCÍA-MAYORAL, R. 2019 Turbulent drag reduction by anisotropic permeable substrates – analysis and direct numerical simulations. *J. Fluid Mech.* **875**, 124–172.

SHANNON, M.A., BOHN, P.W., ELIMELECH, M., GEORGIADIS, J.G., MARI NAS, B.J. & MAYES, A.M. 2008 Science and technology for water purification in the coming decades. *Nature* **452**, 301–310.

SHI, W., ANDERSON, M.J., TULKOFF, J.B., KENNEDY, B.S. & BOREYKO, J.B. 2018 Fog harvesting with harps. *ACS Appl. Mater. Interfaces* **10** (14), 11979–11986.

STEIROS, K. & HULTMARK, M. 2018 Drag on flat plates of arbitrary porosity. *J. Fluid Mech.* **853**, R3.

STEIROS, K., KOKMANIAN, K., BEMPEDELIS, N. & HULTMARK, M. 2020 The effect of porosity on the drag of cylinders. *J. Fluid Mech.* **901**, R2.

STRONG, E.F., PEZZULLA, M., GALLAIRE, F., REIS, P. & SICONOLFI, L. 2019 Hydrodynamic loading of perforated disks in creeping flows. *Phys. Rev. Fluids* **4**, 084101.

THEOFILIS, V. 2011 Global linear instability. *Annu. Rev. Fluid Mech.* **43** (1), 319–352.

VIOLA, F., IUNGO, G.V., CAMARRI, S., PORTÉ-AGEL, F. & GALLAIRE, F. 2014 Prediction of the hub vortex instability in a wind turbine wake: stability analysis with eddy-viscosity models calibrated on wind tunnel data. *J. Fluid Mech.* **750**, R1.

WAGNER, H., WEGER, M., KLAAS, M. & SCHRÖDER, W. 2017 Features of owl wings that promote silent flight. *Interface Focus* **7** (1), 20160078.

WILLERT, C., SCHULZE, M., WALTENSPÜL, S., SCHANZ, D. & KOMPENHANS, J. 2019 Prandtl's flow visualization film c1 revisited. In *13th Int. Symp. on Particle Image Velocimetry*. arXiv: https://elib.dlr.de/128984/1/ISPIV2019_Willert_Paper161.pdf.

WILLIAMSON, C.H.K. 1996 Vortex dynamics in the cylinder wake. *Annu. Rev. Fluid Mech.* **28** (1), 477–539.

ZAMPOGNA, G.A. & GALLAIRE, F. 2020 Effective stress jump across membranes. *J. Fluid Mech.* **892**, A9.

ZAMPOGNA, G.A., PLUVINAGE, F., KOURTA, A. & BOTTARO, A. 2016 Instability of canopy flows. *Water Resour. Res.* **52** (7), 5421–5432.

ZAMPOGNA, G.A. & BOTTARO, A. 2016 Fluid flow over and through a regular bundle of rigid fibres. *J. Fluid Mech.* **792**, 5–35.

ZAMPOGNA, G.A., MAGNAUDET, J. & BOTTARO, A. 2019 Generalized slip condition over rough surfaces. *J. Fluid Mech.* **858**, 407–436.

ZONG, L. & NEPF, H. 2012 Vortex development behind a finite porous obstruction in a channel. *J. Fluid Mech.* **691**, 368–391.